

INSIGHTS FROM SYNTHETIC STAR-FORMING REGIONS:
I. RELIABLE MOCK OBSERVATIONS FROM SPH SIMULATIONS

CHRISTINE M. KOEPFERL^{1,2}, THOMAS P. ROBITAILLE^{1,3}, JAMES E. DALE⁴, AND FRANCESCO BISCANI¹

¹ Max Planck Institute for Astronomy, Königstuhl 17, D-69117 Heidelberg, Germany

² Scottish Universities Physics Alliance (SUPA), School of Physics and Astronomy, University of St Andrews
North Haugh, St Andrews, KY16 9SS, UK

³ Freelance Consultant, Headingley Enterprise and Arts Centre, Bennett Road Headingley, Leeds LS6 3HN

⁴ University Observatory Munich, Scheinerstr. 1, D-81679 Munich, Germany

(Received 29 January 2016; Accepted 1 March 2016)

The Astrophysical Journal Supplement

ABSTRACT

Through synthetic observations of a hydrodynamical simulation of an evolving star-forming region, we assess how the choice of observational techniques affects the measurements of properties which trace star formation. Testing and calibrating observational measurements requires synthetic observations which are as realistic as possible. In this part of the paper series ([Paper I](#)), we explore different techniques for how to map the distributions of densities and temperatures from the particle-based simulations onto a Voronoi mesh suitable for radiative transfer and consequently explore their accuracy. We further test different ways to set up the radiative transfer in order to produce realistic synthetic observations. We give a detailed description of all methods and ultimately recommend techniques. We have found that the flux around 20 μm is strongly overestimated when blindly coupling the dust radiative transfer temperature with the hydrodynamical gas temperature. We find that when instead assuming a constant background dust temperature in addition to the radiative transfer heating, the recovered flux is consistent with actual observations. We present around 5800 realistic synthetic observations for *Spitzer* and *Herschel* bands, at different evolutionary time-steps, distances and orientations. In the upcoming papers of this series ([Paper II](#), [Paper III](#) and [Paper IV](#)), we will test and calibrate measurements of the star-formation rate (SFR), gas mass and the star-formation efficiency (SFE) using our realistic synthetic observations.

1. INTRODUCTION

Over the last decade, progress in the field of star formation has been fueled by an increasing number of large infrared/optical surveys of our Galaxy (e.g. from space missions, such as *Hubble*, *Spitzer*, *Herschel*, *Planck*, and ground missions, such as Two Micron All-Sky Survey (2MASS), UKIRT Infrared Deep-Sky Survey (UKIDSS) and ATLASGAL and a growing number of state-of-the-art simulations of entire star-forming regions with increasing quality and diversity (e.g. ORION, SPH-NG, AREPO; for more details and recent application, see e.g. [Offner et al. 2012](#), [Bate 2014](#), [Springel 2010a](#)). Thanks to recent advances in radiative transfer techniques (in particular 3-d Monte-Carlo radiative transfer; for more details, see the review of [Steinacker et al. 2013](#)) we are now able to produce synthetic observations of star-forming regions. Synthetic observations have the potential, when constructed with great care and effort, to close the loop between simulations and observations. Through **synthetic observations**:

1. On the one hand, simulations can be tested to see whether they reproduce features seen in observations. Whether certain physical processes are dominant over other processes can be tested with synthetic observations by comparing the mock observations of simulated parameter studies to real observations.
2. On the other hand, synthetic observations allow us

to test and calibrate techniques that are used by the community to infer properties related to star formation. Since the intrinsic properties of the simulations (e.g. SFRs, gas masses, filament widths) are known, the accuracy of the observational determination can be explored. Such an approach enables us also to improve existing techniques and to develop new techniques that can produce better measurements.

Lately, there have been many attempts to use synthetic observations with respect to their potential listed above. For example, [Kurosawa et al. \(2004\)](#) used one small-scale simulation of a star-forming region from [Bate et al. \(2002a,b, 2003\)](#). They mapped their initial particle-based simulation output onto an Adaptive Mesh Refinement (AMR) grid and included the density profile of a protoplanetary disk close to their stellar accretion particles (represented by sink particles, for more details on sink particles see [Bate et al. 1995](#)). With their parameter study that included set-ups with and without accretion disks, they developed classification criteria for accretion disks in the mid-infrared (MIR).

[Offner et al. \(2012\)](#) also used a simulation of a small-scale star-forming region to estimate the quality and reliability of properties inferred for protostars from SED-fitting techniques. In contrast to [Kurosawa et al. \(2004\)](#), they did not refine the input density of the simulation further, e.g. with a protoplanetary disk, since the original resolution was sufficient to recover the flux of contributing regions, while unresolved regions were too opti-

cally thick to produce flux in the "observed" wavelength bands.

Up until now, most studies with synthetic observations have focused on simulations of star-forming regions below the pc-scale. Moreover, usually only one snapshot from a simulation is tested, rather than several evolutionary time-steps of the same simulation for different orientations and distances, which would improve the reliability of the conclusions.

We believe that the sequence of simulations initiated by Dale & Bonnell (2011) is a good choice for producing and exploring the applications of synthetic observations, since they cover large-scale single star-forming regions with sizes on the order of several tens of pc. The initial simulation in this sequence of many published SPH simulated star-forming regions covered only one simulated star-forming cluster which satisfies the modified¹ Larson (2005) EOS with an isothermal dust cooling part at 7.5 K and a line cooling process, but lacks stellar feedback mechanisms such as heating through radiation, ionization² & winds. This initial simulation was extended by different high-mass stellar feedback mechanisms, such as ionization (see Dale et al. 2007 for the formalism), introduced by Dale et al. (2012) for bound and Dale et al. (2013a) for unbound clouds. Further, Dale et al. (2013b) introduced winds as feedback of bound and unbound clouds (see Dale & Bonnell 2008 for the formalism). A combination of the initial high-mass stellar feedback parameter study (ionization & wind) for bound and unbound clouds was presented by Dale et al. (2014). With this large set of simulations, these authors are studying the impact of feedback on the star-forming regions. For example, in Dale et al. (2014), they compare the effects of different feedback mechanisms on the SFR and SFE. For simplicity, we will hereafter refer to this set of simulations as the D14 SPH simulations.

In this paper, hereafter referred to Paper I, we will produce realistic synthetic observations of a simulated star-forming region at different stages of evolution, orientations and distances from the D14 SPH simulations. We use the 3-d dust continuum Monte-Carlo radiative transfer code HYPERION, developed by Robitaille (2011), to produce ideal synthetic observations. HYPERION uses a gridded density distribution. In the radiative transfer code, photon packets are emitted from the stellar sources and travel through the density distribution and interact with the dust. They can get scattered, absorbed or re-emitted by the dust grains. HYPERION calculates the specific energy absorbed by the dust resulting from this stellar heating and estimates the dust temperature, and ideal synthetic images can be produced. For more details about HYPERION and radiative transfer in general see Robitaille (2011) and Steinacker et al. (2013).

1.1. Motivation

In this paper (Paper I), we will describe the set-up and the post-processing of radiative transfer models using particle-based simulations as input. Note that we will

¹ The equation of state (EOS) has been adjusted to recover a Jeans mass M_{Jeans} of $0.5 M_{\odot}$.

² Dale & Bonnell (2011) also had an ionization description implemented but the impact was rather small because their simulated region had a large escape velocity.

TABLE 1
SUMMARY OF PROPERTIES
OF THE *run I* SIMULATED STAR-FORMING REGION.

time-step (ID)	time (Myr)	$r(M_{1/2})$ (pc)	sink particles	M_{gas} (M_{\odot})	feedback on?
024	3.576	8.45	3	9873	no
025	3.725	8.52	4	9825	no
026	3.874	8.60	12	9750	no
027	4.023	8.70	15	9664	no
028	4.172	8.77	17	9593	no
029	4.321	8.83	21	9536	no
030	4.470	8.89	30	9476	no
031	4.619	8.94	32	9414	no
032	4.768	9.01	44	9341	no
042	4.917	9.08	48	8833	yes
052	5.066	9.27	48	8643	yes
062	5.215	9.58	53	8598	yes
072	5.364	9.91	61	8495	yes
082	5.513	10.30	73	8377	yes
092	5.662	10.79	85	8187	yes
102	5.811	11.30	91	7987	yes
112	5.960	11.84	98	7722	yes
122	6.109	12.37	100	7500	yes
132	6.258	12.94	108	7254	yes
142	6.407	13.50	115	6996	yes
152	6.556	14.09	122	6687	yes
162	6.705	14.69	125	6409	yes
172	6.854	15.33	128	6105	yes

not focus on the calculations with the radiative transfer code itself. Rather we will explore different methods for how to set up the radiative transfer using the data from the SPH simulations and in order to produce realistic synthetic observations from the radiative transfer output. We go through this effort, so that we can find reliable techniques, to recover the infrared flux as accurately as possible, which is commonly used by observers to interpret star-forming regions.

1.2. Outline

In Section 2, we will introduce the D14 SPH simulations in more detail, show the evolution of properties over the relevant time-steps and justify the pre-processing steps to make the simulation sample suitable for the radiative transfer set-up. In Section 3, we will present different approaches for discretizing an SPH simulation onto a radiative transfer grid such as a Voronoi mesh. Aspects of setting up radiative transfer photon sources are discussed in Section 4, before the careful set-up of circumstellar material is described in Section 5. In Section 6, different dust properties and temperature combinations and their effects on the radiative transfer output are explored. We give suggestions in the respective sections on which of the methods (explored in Section 2 to Section 6) to favor. The post-processing of the radiative transfer output is described in Section 7 and the resulting realistic synthetic observations are presented there. In Section 8, we summarize caveats when transferring simulations to "observations".

In (Koeperl et al. 2016a, submitted) and (Koeperl et al. 2016b, submitted), hereafter referred to Paper II and Paper III, we use the resulting realistic synthetic observations at different evolutionary stages to test and calibrate techniques which measure properties, such as the SFR, the gas mass and the SFE.

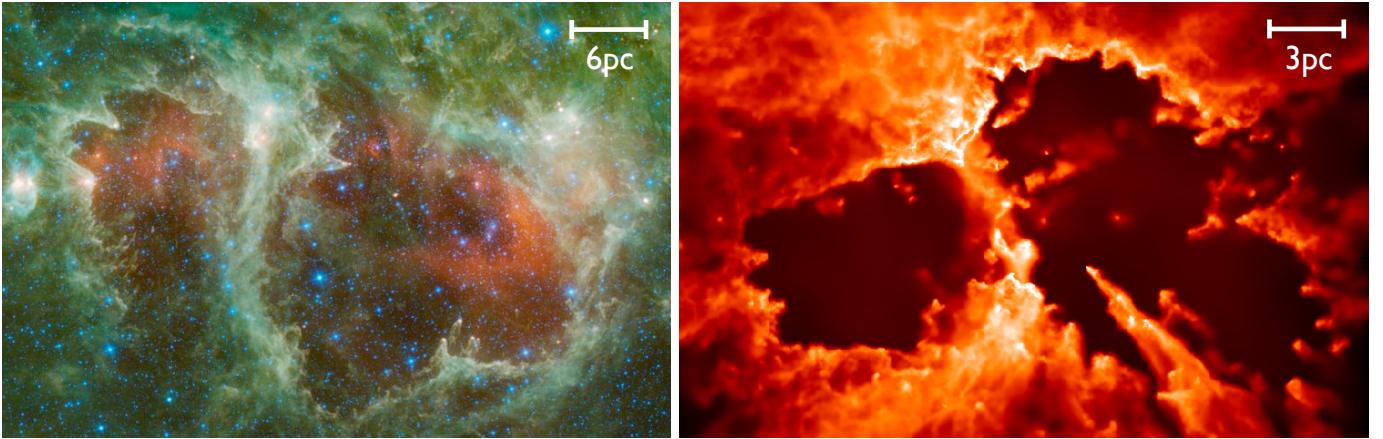


FIG. 1.— (Left) MIR Wide-field Infrared Survey Explorer (WISE) observation^a of the Soul Nebula star-forming region (blue: 3.4 μm , cyan: 4.6 μm , green: 12 μm , red: 22 μm), (right) column density structure of a simulated star-forming region from the D14 smoothed particle hydrodynamics (SPH) simulations^b with high-mass stellar feedback (ionization-only).

^aOnline references accessed: 30.08.2015; <http://www.jp1.nasa.gov/spaceimages/details.php?id=PIA13112>
 Courtesy NASA/JPL-Caltech/UCLA

^bSurface density maps provided by Jim Dale.

2. HYDRODYNAMICAL SIMULATIONS

The D14 SPH simulations are a set of over 20 different realizations with different initial conditions for initially bound and unbound star-forming regions. Furthermore, for every realization, different combinations of high-mass stellar feedback mechanisms, such as ionization alone, winds alone, winds & ionization coupled, are calculated. The morphological features and physical scale of the simulations (half-mass radii $r(M_{1/2})$ from 1 pc to 100 pc) are of the same order as those of observed regions with high-mass star formation in the Galactic plane. This can be seen in Figure 1, where we show a three-color MIR WISE observation of the Soul Nebula (left, Koenig et al. 2012; Wright et al. 2010) and the column density structure of one snapshot from the D14 SPH simulations including high-mass stellar feedback in form of ionization (right). As mentioned in Section 1, the D14 SPH simulations are in some sense unique in the community since they cover single star-forming regions on large scales of the order of several tens of parsec with different feedback scenarios.

2.1. Simulation Properties

The density distribution in particle-based simulations, such as the D14 SPH simulations, is approximated by the sum of many individual SPH particles with an analytical description.

2.1.1. SPH Particles

From the simulation output, we know the position of an SPH particle i , its peak density $\rho_{i,\text{SPH}}$, its hydrodynamical gas temperature $T_{i,\text{SPH}}$, its constant particle mass of $m_{i,\text{SPH}} = 10^{-2} M_{\odot}$ ³ and its smoothing length h_i . A SPH particle i has a 3-d Gaussian-like profile. The profile strength at position j with distance r_{ij} from the SPH particle i is defined by the kernel function (for a

detailed review, see Springel 2010b):

$$W_{ij}(r_{ij}, h_i) = \frac{1}{h_i^3 \pi} \times \begin{cases} 1 - 1.5(r_{ij}/h_i)^2 + 0.75(r_{ij}/h_i)^3 & \forall r_{ij} < h_i \\ 0.25(2 - (r_{ij}/h_i))^3 & \forall h_i \leq r_{ij} < 2h_i \\ 0 & \forall r_{ij} > 2h_i \end{cases} \quad (1)$$

2.1.2. Sink Particles

The stellar particles in an SPH simulations are represented by sink particles (Bate et al. 1995). They form from SPH particles which are bound by the gravitational potential of a forming stellar object and follow the following conditions:

- **Density Threshold**

The density threshold is evaluated from the minimal resolvable Jeans mass M_{Jeans} and the isothermal temperature in the simulations. SPH particles, which have higher densities than the threshold density, are tracked and the nearest neighbors are tested by the following conditions.

- **Jeans Limit**

The average density and temperature of the group of SPH particles. The resulting mean total mass of the group should be higher than the Jeans mass M_{Jeans} .

- **Potential**

The group should be gravitationally bound.

- **Velocity Field**

The group should have a negative divergence of the velocity field at the location of the densest particle of the group which indicates a collapse.

- **Energy Balance**

The group of collapsing SPH should also have a higher gravitational energy than its rotational kinetic energy to ensure that the collapse cannot be stabilized by angular momentum conservation.

³ This is only true for the simulated clouds with a total mass of $M_{\text{cloud}} = 10^4 M_{\odot}$ for instance run I, since $m_{i,\text{SPH}} = M_{\text{cloud}}/N_{\text{SPH}}$, with the total SPH particle number N_{SPH} being $1e6$.

In the D14 SPH simulations, a sink particle forms once more than 50 SPH particles satisfy the above conditions at a given position. In Table 1 we give the number of sink particles at different time-steps in one of the D14 SPH simulations.

From the minimum resolved Jeans mass M_{Jeans} , a respective length scale, called the accretion radius r_{acc} , is calculated, which is comparable to the Jeans length λ_{Jeans} . SPH particles are accreted by a sink particle when they are within the accretion radius r_{acc} , are gravitationally bound by the sink particle’s potential and have low enough rotational energies. The sink particles⁴ grow over time through accretion of many SPH particles.

2.1.3. Feedback

High-mass stellar feedback is switched on in the D14 SPH simulations as soon as three high-mass sink particles above $20 M_{\odot}$ have formed⁵. The simulation ends before the first supernova of a high-mass sink particle would presumably go off.

2.1.4. Run I

In this work, we explore the *run I* of the D14 SPH simulations an intermediate mass cloud with a total gas mass of $10^4 M_{\odot}$ and initially 10^6 SPH particles. We choose this run because it is of relatively high resolution with a sink accretion radius of $r_{\text{acc}} = 0.005$ pc. Individual stellar objects in the form of sink particles with masses between $0.5 M_{\odot}$ and $70 M_{\odot}$ are produced and can be resolved, and therefore can be interpreted as single stars. The first stars formed after about 3.6 Myr after the start of the simulation (see also Section 2.1.6). The stars in the simulation grow through accretion (see also Section 2.1.7) and ensures that the stellar population acquires its own initial mass function (IMF) without imposing an initial IMF to the simulation (see Dale et al. 2012).

We choose *run I* because we aim to produce synthetic observations which are as close to real star-forming regions as possible. Therefore, for our studies, we limit ourselves to the coupled feedback scenario: ionization & winds. The ionizing sources in the simulations emit a flux of ionized photons ranging from $1.3 \times 10^{48} \text{ s}^{-1}$ to $1.0 \times 10^{49} \text{ s}^{-1}$. They also emit winds⁶ with a speed ranging from 1780 km s^{-1} to 3125 km s^{-1} and a respective mass-loss rate between $3.1 \times 10^{-7} M_{\odot} \text{ yr}^{-1}$ to $2.8 \times 10^{-6} M_{\odot} \text{ yr}^{-1}$. For a detailed description of the high-mass feedback formalism, see Dale (2015); Dale et al. (2013b, 2012); Dale & Bonnell (2008); Dale et al. (2007).

In *run I* the first stars formed after about 3.6 Myr, high-mass stellar feedback is switched on about 4.8 Myr and the simulation is stopped at about 7 Myr after the start of the simulation. The simulation is stopped before the first supernova⁷ would presumably go off. We select

⁴ For the intermediate mass clouds of the D14 SPH simulations sink particles as low as $0.5 M_{\odot}$ can be formed and the sink particles and represent stars. For clouds above $10^5 M_{\odot}$, which are not subject of this paper, sink particles represent subclusters.

⁵ This is only true for intermediate mass clouds below $10^5 M_{\odot}$ in the D14 SPH simulations.

⁶ only modeled as momentum fluxes

⁷ Note that the supernova explosion is not part of the D14 SPH simulations. For further information about the supernova (e.g. timing) see the D14 SPH simulations.

23 time-steps with a constant step size $\Delta t = 149\,000$ yr, starting once the first star has formed. At every time-step t_{step} and for every sink particle, we keep track of the physical properties, such as the sink particle mass $M_{\text{sink}}(t_{\text{step}})$, the age of the sink particle $t_{\text{age}}(t_{\text{step}})$ and the accretion rate $\dot{M}_{\text{acc}}(t_{\text{step}})$. For more details see Table 1.

2.1.5. Sink Particle Mass

The sink particle mass is defined as the sum over all N_{acc} accreted SPH particles i :

$$M_{\text{sink}}(t_{\text{step}}) = \sum_{i=1}^{N_{\text{acc}}} m_{i,\text{SPH}}. \quad (2)$$

2.1.6. Sink Particle Age

Hereafter, we define the age of a sink particle as

$$t_{\text{age}}(t_{\text{step}}) = t_{\text{step}} - t_{\text{appear}} + \Delta t/2, \quad (3)$$

where t_{appear} is the time of the time-step when a sink particle first forms (binds more than 50 SPH particles). We add the time $\Delta t/2$ to the age because the sink particle may have formed at any time between the time-step when it appeared and the previous one, and therefore on average we assume that it formed half way in between the two.

2.1.7. Sink Accretion Rate

We consider a sink particle to be accreting between two different time-steps, when

$$\text{accretion}|_{t_{\text{step}} \rightarrow t_{\text{step}+1}} = M_{\text{sink}}(t_{\text{step}+1}) > M_{\text{sink}}(t_{\text{step}}). \quad (4)$$

The accretion definition becomes important when mapping the SPH simulation to the Voronoi mesh as described in Section 3. We define the accretion rate at a time t_{step} as the mass-gain rate between two time-steps:

$$\dot{M}_{\text{acc}}(t_{\text{step}}) = \frac{M_{\text{sink}}(t_{\text{step}+1}) - M_{\text{sink}}(t_{\text{step}-1})}{2\Delta t}. \quad (5)$$

2.2. Pre-processing the SPH Simulation Output

In subsequent sections, we want to extract high-resolution radiative transfer images (see Section 7) with constant pixel number and pixel-size scale over all time-steps. Since we are only interested in the inner region of the simulation, we spatially clip the simulations in order to save computational resources. The clear trade-off is that we are then not always tracing the same amount of mass in each time-step.

We clip the D14 SPH simulation output in physical size to a cube with length 30 pc. For the first time-steps, the star-forming region is completely contained inside the box; once the high-mass stellar feedback has been switched on, the region expands beyond the boundaries of the cube. In the final time-steps, the boundaries of the cube are approximately the half-mass radius $r(M_{1/2})$ of the simulations. More detailed values are provided in Table 1, where we summarize some properties of *run I* at every time-step.

In the following, we investigate two possible selection methods to single out the appropriate sample of SPH particles for the respective radiative transfer set-up:

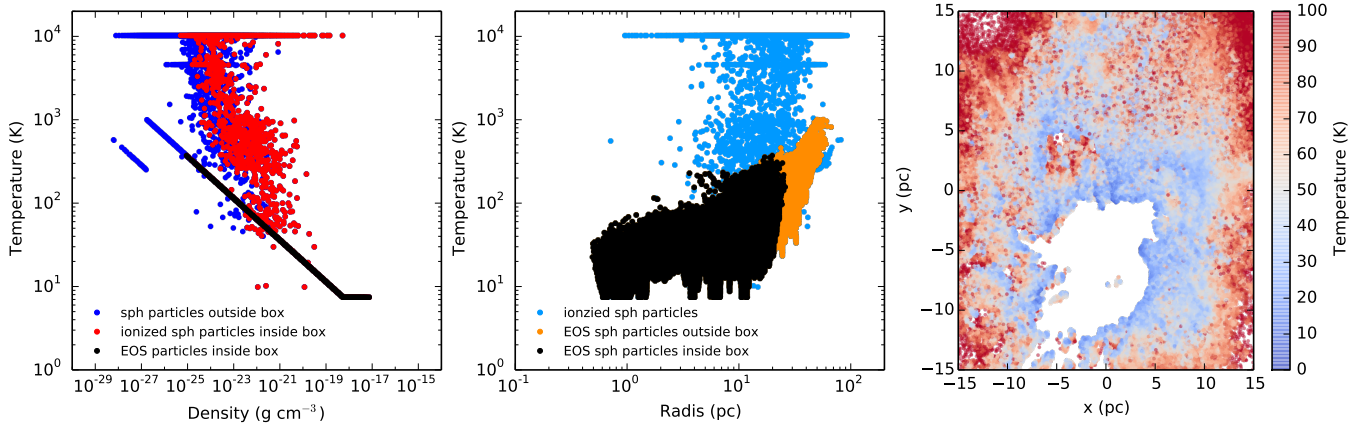


FIG. 2.— Temperature relation in density and radius of SPH particles and a 2-d projection showing the temperature increase at the edges of the simulation at time-step 122 (6.109 Myr).

2.2.1. Method c1 — Neutral SPH Particles in Box

While the D14 SPH simulations have high-mass stellar feedback mechanisms implemented, the simulations do not take into account the dust heating from the stars. In D14 SPH simulations, the external heating through the diffuse Galactic radiation field is approximated by the Larson (2005) EOS⁸ rather than just an isothermal approximation. The EOS contains the following regimes (following Equation 1 and Figure 1 of Dale et al. 2012):

- line cooling processes

$$P \sim \rho^{3/4} \quad (6)$$

$$\forall \rho < 5.5 \times 10^{-19} \text{ g cm}^{-3}$$

- dust cooling processes

$$P \sim \rho^{1.0} \quad (7)$$

$$\forall 5.5 \times 10^{-19} \text{ g cm}^{-3} < \rho < 5.5 \times 10^{-15} \text{ g cm}^{-3},$$

where P is the gas pressure and ρ the gas density. Since in the ideal gas approximation (see Feynman 1977), the pressure P always follows

$$P = Nk_B T / V = \rho k_B T / m_p \sim \rho T, \quad (8)$$

with gas particle number N , the Boltzmann constant k_B , the gas temperature T , the gas particle mass m_p and the gas Volume V , we can also express the line cooling term from Eq. 6 as a power-law of density ρ and temperature T :

$$P \sim \rho T \sim \rho^{3/4} \rightarrow \rho \sim T^{-4}. \quad (9)$$

At high densities, dust cooling is assumed to dominate and the EOS becomes isothermal with $T_{\text{iso}} = 7.5$ K. The densities in large parts of the cloud are low enough that the gas and dust should not be well coupled thermally.

In Figure 2(a), we have plotted temperature versus density for time-step 122 (at 6.109 Myr) of run I 1.341 Myr after switching on high-mass stellar feedback (c.f. Table 1). Points regardless of color (blue, red and black points together) represent all 10^6 SPH particles of run I. The red and black points represent SPH particles

which lie within our selected box of 30 pc width. The red points are (partly or fully) ionized particles (c.f. with Dale et al. 2012, 2007) within the box. The horizontal line at 10^4 K shows all the fully ionized SPH particles. The other red points are partly ionized and lie within the selected box. The black points are neutral SPH particles in the selected box. The state of these neutral particles is described by the EOS which is describing the dependency of density and temperature (diagonal line: Eq. 6, Eq. 8, Eq. 9; horizontal: Eq. 7).

In this work, we will use a dust radiative transfer code, therefore we will only use SPH particles in the box which are completely neutral since dust gets destroyed during the ionization process (Diaz-Miller et al. 1998). Hereafter, we call the clipping for size and only neutral SPH particles, resulting in the black particles in Figure 2(a), method c1.

2.2.2. Method c2 — Neutral SPH Particles in Box & Temperature Limit

In Figure 2(b), we can see that the SPH temperature increases with radius from the center of the simulation. Hot ionized particles (cyan) move to larger radii, but SPH particles that still follow the EOS also have higher temperatures at larger radii. This is a result of the EOS, since the density decrease with radius in the centrally-condensed clouds. These can also be seen in Figure 2(b) and the 2-d temperature plot of Figure 2(c), where we only plot the black sample of Figure 2(a,b). The maximum temperature at the boundary of the box at this time-step lies around 400 K.

The SPH temperature of neutral particles in the box is lower than the typical dust sublimation temperature of 1600 K (e.g. Whitney et al. 2003), but much higher than the expected ambient dust temperature around a star-forming region of about 18 K (see Paper II). We explore further temperature cuts of the line cooling part of the EOS. Hereafter, we call the clipping in size using only neutral particles, and removing particles above a certain threshold temperature clipping, method c2. Note that method c2 is the same as c1, but additionally particles above a certain threshold temperature are removed.

2.2.3. Results — Pre-processing

In Figure 3, we show the temperature histogram of neutral particles with a box of 30 pc of the four time-

⁸ The EOS has been adjusted by the D14 SPH simulations of intermediate clouds to recover a Jeans mass M_{Jeans} of $0.5 M_{\odot}$.

steps 024 (3.576 Myr), 032 (4.768 Myr), 072 (5.364 Myr) and 122 (6.109 Myr). We can see that the temperature peak shifts from $T = 60$ K to about $T = 35$ K once the high-mass stellar feedback is turned on after time-step 32 (4.768 Myr). This is due to the sweeping up of the low-density neutral gas into dense, cool clumps.

Therefore, a clipping, and hence removing of the SPH particles above a certain temperature (e. g. 60 K) in clipping method c2, is not helpful, since we would lose too many particles for certain time-steps. Also, a threshold temperature below the sublimation is hard to pick, since it remains unclear when exactly the temperature of the dust decouples from the temperature of the gas. Hereafter, we will only remove non-neutral SPH particles from the simulation, as in clipping method c1, and keep SPH particles at all temperatures within the box, which is always below the sublimation temperature.

Note that such a steep increase in temperature with radius is not observed in the dust species of real star-forming regions. Hence, implementing the hydrodynamical temperature which is a result of the line cooling part (Eq. 6) of the EOS, and therefore gas phase of the region, should happen with caution. We will address this in detail in Section 6, where we present a better treatment of the dust temperature.

3. GRID

To create realistic synthetic observations we use HYPERION, a 3-d dust continuum Monte-Carlo radiative transfer code (Robitaille 2011).

3.1. Different Grids

HYPERION and other Monte-Carlo radiative transfer codes use density and temperature structures that are discretized onto grids. The right choice of grid is very important in terms of recovering the dynamical range of the input structure and in terms of computational efficiency. HYPERION has a variety of grid types implemented.

Regular Cartesian grids become inefficient when mapping a particle distribution onto a high-resolution grid to recover the dynamic range of a large-scale simulation box. Cartesian related grids, such as Octree grids or Cartesian AMR grids, can improve the calculation by providing higher resolution in certain regions and can recover the dynamic range of the density structure in the simulation. But these grids are orientation dependent which can cause observational artifacts when observing along the axes. For example, "observations" along the Cartesian axes will make the edges of a cell visible.

The Voronoi tessellation (for more details, see Camps et al. 2013; Springel 2010a) is a type of irregular grid where each cell is described by an irregular polyhedron. Every polyhedron is set up by a point in 3-d space, which we refer to as a *site* from now onwards. The boundaries of the polyhedra are defined by the set of points that are closest (hence, nearest neighbors see Press et al. 1992) to the site. The polyhedra have no preferred direction and resolution can be increased by adding more Voronoi sites, which enables us to represent large dynamic ranges. Therefore, mapping particle-based simulations onto a mesh using a Voronoi mesh⁹ is beneficial for our proposes. Note, Mapping SPH simulations onto a

Voronoi mesh has also been carried out by Hubber et al. (2016), Barcarolo et al. (2014), Starinshak et al. (2014) and Zhou et al. (2007).

Since the primary goal of this paper is to produce reliable synthetic observations of star-forming regions we choose an approach which follows the following condition set by the radiative transfer calculation:

- satisfactory resolution around the forming stars
- mapped simulation properties follow the gradient of simulation properties
- number of cells manageable by the radiative transfer calculation

In order to fulfill the above requirements we can not refine the output of the SPH simulation before assigning the Voronoi sites. Otherwise we would produce too many cells. Therefore we need to construct the Voronoi sites first (see Section 3.2) before calculating the resulting properties (see Section 3.3) of the found sites.

3.2. Voronoi Sites

Choosing the Voronoi sites of the tessellation wisely is one of the critical elements when setting up a Voronoi mesh efficiently. While a rule of thumb is that regions with higher densities should have higher resolution and hence more sites, one has to keep in mind that very optically thick regions will trap photons and many such cells are not beneficial to the radiative transfer calculation (for a discussion of this, see Camps et al. 2013). In Figure 4, we plot density slices of different site distributions within a box of 1 pc and highlight accreting sink particles in red and sink particles in the ionizing bubble in blue. The actual evaluation of the density in the cells will be described in Section 3.3. In this section, we only focus on the changes of the cell sizes when using three different methods of distributing the sites in the Voronoi mesh:

3.2.1. Method s1 — Sites at SPH Particle Position

A first order approach is, to put sites at the positions of the SPH particles of the clipped sample c1 (for details about the sample selection, see Section 2.2). Hereafter, the site method s1 is defined by sites at SPH positions alone. While this works rather well for isolated sink particles (see sink particle 110753 in Figure 4(a)), very large high-density Voronoi cells are created close to the ionizing bubble (see 11640 and 197247 in Figure 4(a)). These large high-density cells are an artifact of the SPH to Voronoi mesh mapping and were not part of the initial simulations. Artificial high-density regions create overestimated fluxes in the radiative transfer because now very large high-density regions lie close to very luminous objects.

3.2.2. Method s2 — Sites at SPH & Sink Particle Position

In Figure 5, we show the radial peak density distribution of SPH particles close to sink particles for an accreting source in a small cluster (11640), an isolated accreting source (110753) and a source in the ionizing bubble

HYPERION by Thomas Robitaille and Francesco Biscani using the VORO++ library (Rycroft 2009).

⁹ The Voronoi tessellation has been recently implemented into

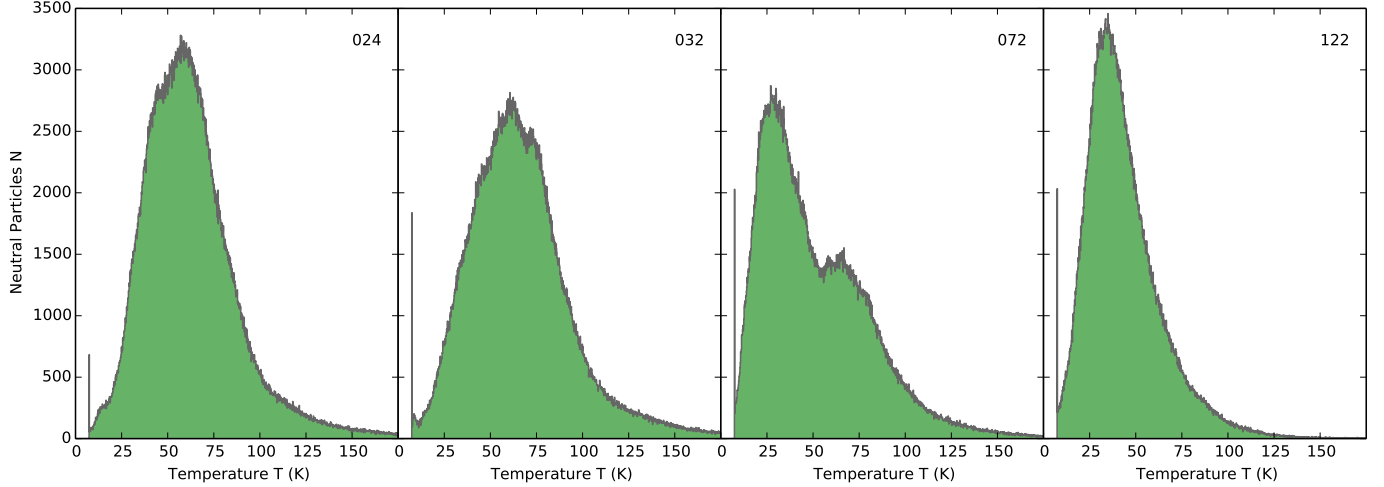


FIG. 3.— Temperature histogram of neutral SPH particles for time-step 024 (3.576 Myr), 032 (4.768 Myr), 072 (5.364 Myr) and 122 (6.109 Myr). Feedback gets switched on after time-step 32. The sharp spikes at 7.5 K are SPH particles in the isothermal phase.

(115358), which lost all its material due to a close-by ionizing source; all profiles of all sources are displayed in the online extension of Figure 5. Red vertical lines highlight the distance of nearby accreting sink particles, while blue lines highlight nearby sink particles in the ionizing bubble. We can see that accreting sources can cause a radial trend in the distribution of the SPH particles, which can be seen very clearly for sink particle 110753 directly in Figure 5 (middle), but also for the density peaks in the density profile at 1 pc distance of sink particle 11640 in Figure 5 (middle) and of sink particle 110753 in Figure 5 (left).

Ionizing sources create (large) voids in the profile (for 115358 about 0.6 pc). Physically, this void represents ionized low-density bubbles around the ionizing stars. Since there is a low-density region around the ionizing sink particles, very few SPH particles are located close to the other sink particles in the ionizing bubble. For example, the closest SPH particle to sink particle 115358 is about 0.6 pc away.

The Voronoi cells around the sink particles are created by distant SPH particles beyond the bubble which have a higher density than the bubble. When ionizing sources are present in the particle-based simulation, artificial large density cells can be avoided by putting additional sites at the positions of the sink particles. Hereafter, we will refer to this method as site method s2, which combines sites at the position of the SPH particles and the sink particles.

When adding sites at the position of the sink particles, we can reproduce the low-density bubbles around the ionizing sink particles. And hence, the size of high-density cells reaching inside the bubbles is truncated. In Figure 4(b), we show this effect for sink particle 11640 and sink particle 197247, which have ionizing bubbles close-by.

3.2.3. Method s3 — Sites at SPH Particle & Sink Particle Position & Circumstellar Sites

When inspecting Figure 4(b), we see that there are still some large high-density cells relatively close to the accreting sink particles, which is partly due to lack of resolution of the SPH simulation. Adding additional circumstellar sites around the accreting sink particles in-

creases the resolution around the accreting sink particles and minimizes the artificial high-density cells as can be seen in Figure 4(c). Hereafter, site method s3 combines sites at the position of SPH particles, the sink particle position and the circumstellar sites around accreting sink particles.

On average, the distance between an accreting sink particle and the closest SPH particle is 0.01 pc which is about 2000 AU as can be seen for the accreting sink particles 11640 and 110753 in Figure 5 (left, middle). Concretely, in the method s3 set-up, the position of the sites is constructed using a constant probability distribution function (PDF) (for more details, see Appendix B and Press et al. 1992) in log-space of radius:

$$r = 10^{\xi[\log_{10} r_{max} - \log_{10} r_{min}] + \log_{10} r_{min}}, \quad (10)$$

with $r_{min} = 10^{-4}$ pc and $r_{max} = 10^{-1}$ pc. The angles θ and ϕ are spaced isotropically within the sphere:

$$\theta = \arccos(2\xi - 1) \quad (11)$$

$$\phi = 2\pi\xi. \quad (12)$$

Once we set the circumstellar sites of method s3 in this way, we can approximate the density gradient of the envelope more smoothly. This will be discussed in more detail in Section 5.1.

3.2.4. Results — Voronoi Sites

In this section, we already explained in detail different methods of how to distribute the sites in a Voronoi mesh with a particle-based code as input. Site distribution method s3, with sites at the neutral SPH positions, at the sink particle positions and circumstellar sites around the accreting sink particles, can increase the resolution and remove artifacts from the particle to mesh transition. This is why we highly recommend distributing sites in this manner. We found that the number of circumstellar sites $N_{circ} \approx 1000$ is a good estimate to increase resolution around the sink particles but not create too many cells, which might slow down computation for the steps described in the next sections. In the remainder of this paper, we explicitly use the site distribution method s3.

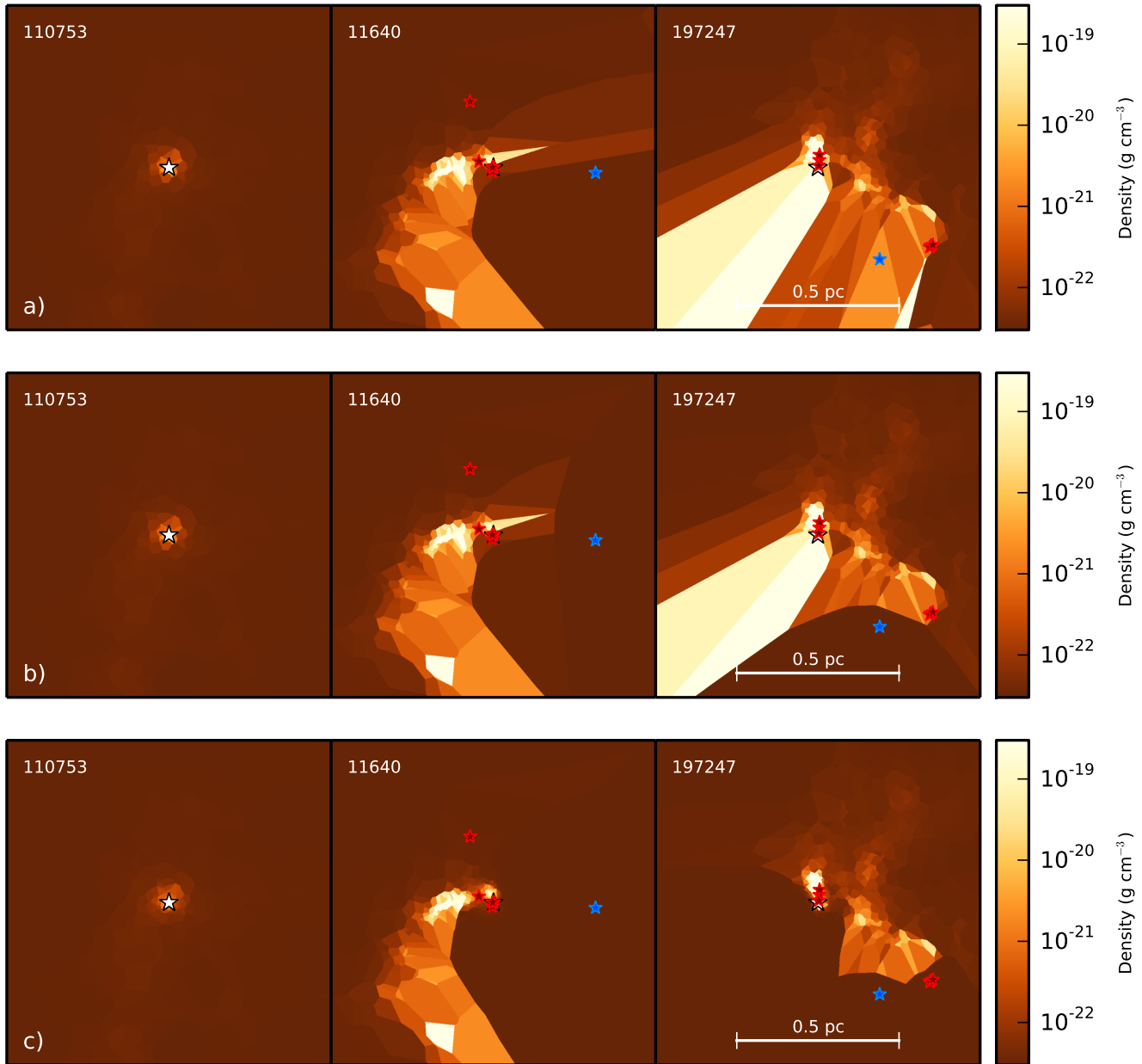


FIG. 4.— 2-d density slices of the Voronoi tessellation with different site methods (s1: top, s2: middle, s3: bottom); (white stars) sink particles with ID; (red stars) accreting sink particles and (blue stars) sink particles in the ionizing bubble within a box of 1 pc length.

3.3. Density and Temperature Mapping onto new Sites

In Figure 4, we showed slices of the density for different site distribution methods. To make the plot we used for the sites coinciding with SPH particle positions the peak density $\rho_{i,\text{SPH}}$ at that position of the SPH particle. When adding sites to a Voronoi mesh, where no SPH particles were located before, we need to evaluate the properties such as density or temperature from the SPH distribution. We need to preserve the density and temperature structure as precisely as possible because later those property meshes will be passed to the radiative transfer set-up. In this section, we will investigate three techniques to map the density distribution onto a Voronoi mesh:

3.3.1. Method p1 — Evaluation of SPH Kernel Function

To evaluate the density at a new site j at the position of the sink particle or at a circumstellar site around a sink particle, we compute the SPH density function (for a detailed review, see [Springel 2010b](#)) for the N closest SPH particles:

$$\rho_{j,\text{p1}} = \sum_{i=1}^N m_{i,\text{SPH}} W_{ij}(r_{ij}, h_i). \quad (13)$$

Where $m_{i,\text{SPH}}$ is the constant SPH particle mass with the value $m_{i,\text{SPH}} = 10^{-2} M_{\odot}$ in *run I* of the D14 SPH simulations and the kernel function $W_{ij}(r_{ij}, h_i)$ from Eq. 1.

We estimate the temperature at a new site j by weighting ([Press et al. 1992](#)) the SPH particle temperature

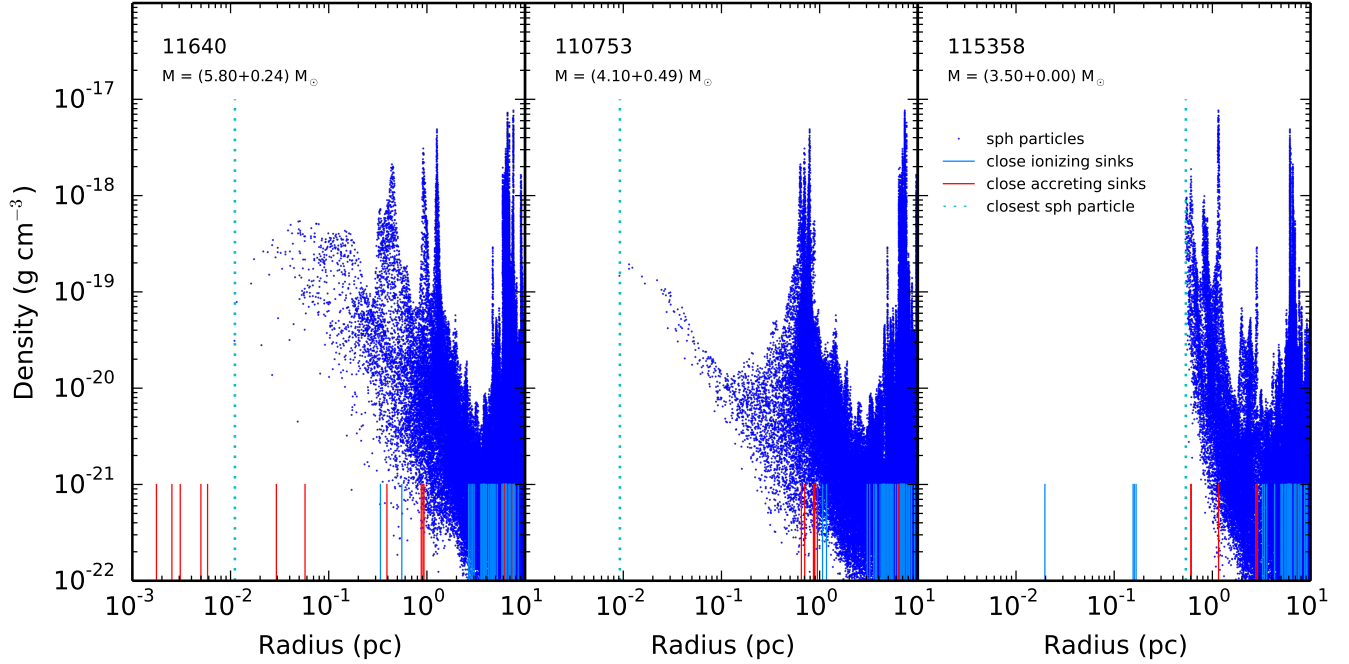


FIG. 5.— Radial density profile in time-step 122 (6.109 Myr): (a) centered on three sink particles: 11640 is an accreting sink particle in a small tight cluster of sink particles; 110753 is an isolated accreting sink particle; 115358 is sink particles in the ionizing bubble which lost all its circumstellar material due to other ionizing sink particles. (b - online material) centered on all sink particles. Red lines highlight the distance of other accreting and blue of sink particles in the ionizing bubble. The dashed cyan line shows the radius of the closest SPH particle to the sink particle.

$T_{i,\text{SPH}}$ of the closest N particles with distance¹⁰ r_{ij}

$$T_{j,\text{p1}} = \frac{\sum_{i=1}^N T_{i,\text{SPH}} m_{i,\text{SPH}} W_{ij}(r_{ij}, h_i)}{\rho_{j,\text{p1}}} \quad (14)$$

with the help of Eq. 13. We explored the effect of setting N to different values and found that setting $N > N_{\text{neighbor}}$ produces a good approximation¹¹ of the exact solution of the density. Hereafter, we call this property evaluation method p1.

In Figure 6(a), we plot the density evaluation with property method p1 and site method s3 (note the different scale than Figure 4(c)). We can see that even with the site distribution method s3, we still have artifacts of large high-density cells as already mentioned in Section 3.2. These large high-density cells are due to the density overestimation when using the peak density $\rho_{i,\text{SPH}}$ at the SPH particles which lie in large cells.

When mapping the density with method p1, we recover a total mass of 139 945 M_{\odot} which is several orders of magnitude to high then the actual mass of about 7500 M_{\odot} . Therefore, we explore other techniques.

3.3.2. Method p2 — Evaluation of Splitted SPH Particles

In the community of SPH modelers, the density is sometimes approximated in Voronoi cells using an average density $\bar{\rho} = m_{\text{SPH}}/V_{\text{cell}}$ (David Hubber, private communication). We do not use this technique, since it can

¹⁰ The temperature can also be evaluated by weighting with the density function. We will explore this in the next section.

¹¹ In run I $N_{\text{neighbor}} = 65$. We found that with $N = 100$, which means that $N > N_{\text{neighbor}}$, we can recover 99.9% of the exact solution.

only be used to evaluate the density in cells containing SPH particles. When adding new sites, this approximation becomes untrue because the volume V_{cell} shrinks, while m_{SPH} remains constant by definition. Also, the density evaluation of cells which contain the new sites is not covered by that technique.

Thus, we virtually split the mass of an SPH particle i according to the 3-d Gaussian-shaped SPH kernel function (see Eq. 1). We repeat this for all SPH particles. Through simple counting, we reevaluate the mass in the cells of the sites j of the existing SPH particle sites plus the newly added sites of method s3. Hereafter, we call this property evaluation method p2.

To space the split SPH particle k with respect to the SPH particle i again, we use a linear spaced PDF (as described in detail in Appendix B) and solve for the positions of the split particles r_{ik} . We distribute the split SPH particles isotropically (see Eq. 11 and Eq. 12). We convert all the $N_{\text{split}}^{\text{p2}}$ split SPH particles to Cartesian coordinates and scale the distance by the respective smoothing length h_i of the SPH particle which got split, since we set $h_i = 1$ for the calculation above. The split SPH particles do not necessarily fall in the cell of the SPH particles they split from. By searching for the nearest neighbor sites (Press et al. 1992) to each split SPH particle, we can now reassess the mass of the Voronoi cells, the split SPH particles fall into. We then calculate the new density $\rho_{j,\text{p2}}$ at a cell site j as

$$\rho_{j,\text{p2}} = \sum_{k=1}^{n_j} m_{\text{SPH},k}/V_j, \quad (15)$$

with the split SPH particle mass $m_{\text{SPH},k} = m_{\text{SPH},i}/N_{\text{split}}^{\text{p2}}$

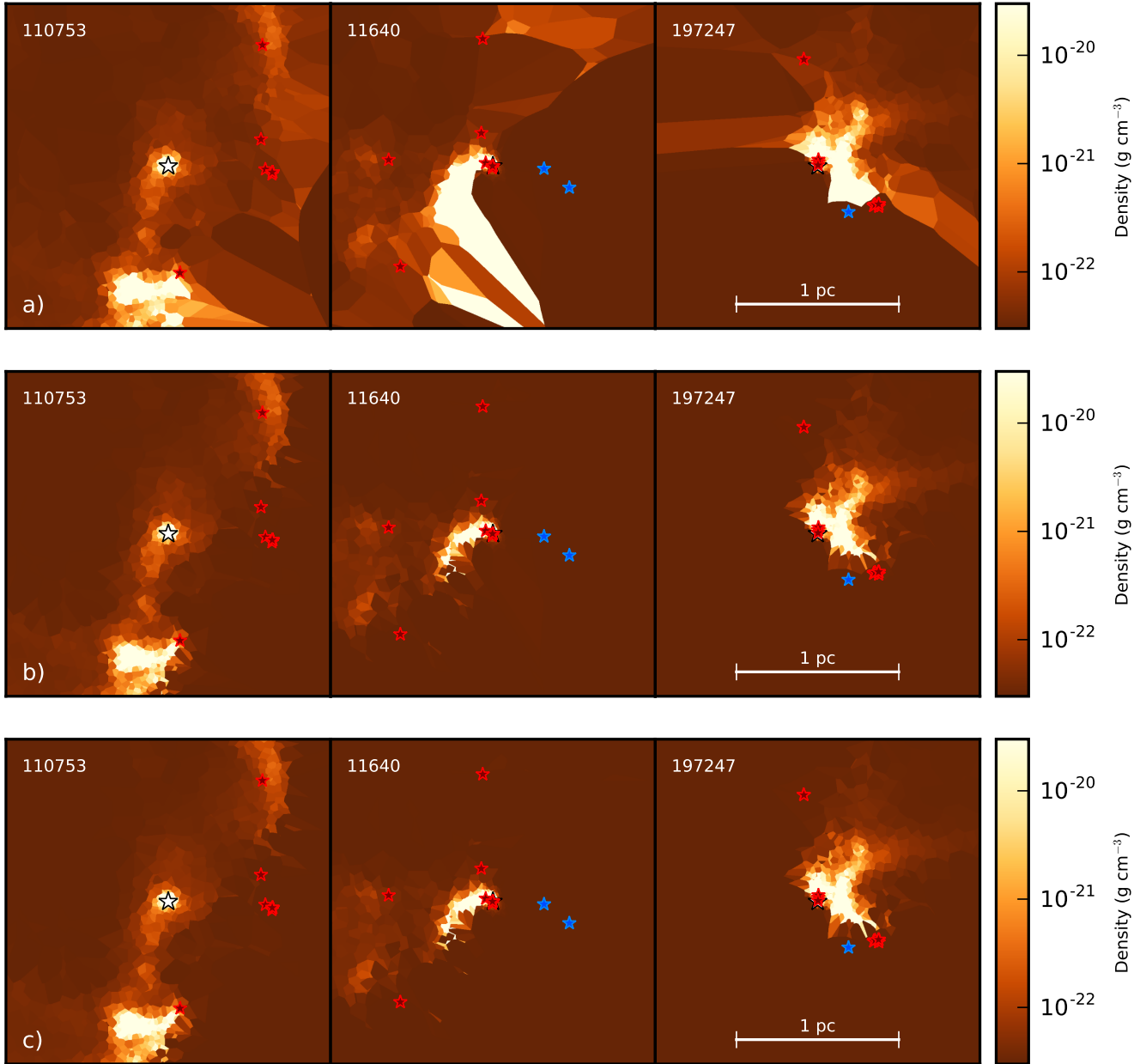


FIG. 6.— Different methods of density translation onto the Voronoi grid (p1: top, p2: middle, p3: bottom); (white stars) sink particles with ID; (red stars) accreting sink particles and (blue stars) sink particles in the ionizing bubble within a box of 2 pc length.

and the number n_j set to the number of split SPH particles found in a cell with the volume V_j . We found that splitting by $N_{\text{split}}^{\text{p2}} = 100$ is a good trade-off between finding a smooth density distribution and computational efficiency.

Since the probability of accumulating many split SPH particles decreases with decreasing cell size, we introduce a threshold of $N_{\text{threshold}}^{\text{p2}} = 10$ split SPH particles. For cells which collect fewer than $N_{\text{threshold}}^{\text{p2}}$, we evaluate $\rho_{j,\text{p1}}$ from Eq. 13.

In Figure 6(b), we plot the density evaluated with property method p2. When comparing to Figure 6(a), one can see that the transition between cells is smoother and artificial high-density Voronoi cells are substantially

fewer.

To evaluate the temperature, we simply keep track from which original SPH particle of mass $m_{\text{SPH},i}$ a split SPH particles of mass $m_{\text{SPH},k}$ comes from and what temperature T_i it had, we can weight the temperature accordingly by the density:

$$T_{j,\text{p2}} = \sum_{k=1}^{n_j} T_i(m_{\text{SPH},k})/n_j. \quad (16)$$

For the cells with $n_j < N_{\text{threshold}}^{\text{p2}}$, we calculate the temperatures as in method p1.

When mapping the density with method p2, we recover a total mass of $7530 M_{\odot}$ relatively close to the real mass of $7500 M_{\odot}$.

3.3.3. Method p3 — Evaluation Using Random Sampling

Another possibility is to evaluate the density by sampling N_{random} random positions l in the grid and calculating the density from the kernel distribution (as in method p1) of the N closest SPH particles to the positions l .

By averaging¹² the density of the random points l at n_j positions in cell j , we get the total density $\rho_{j,p3}$ of method p3

$$\rho_{j,p3} = \sum_{l=1}^{n_j} \rho_{l,p1} / n_j. \quad (17)$$

Typically, we set $N_{\text{random}} \approx 2 \times 10^7$ for $N_{\text{SPH},i} \approx 7 \times 10^5$ neutral SPH particles in the simulation time-step and $N_{\text{split}}^{\text{p3}} = 30$ as above. To ensure that every cell j has at least $N_{\text{threshold}}^{\text{p3}} = 20$, we add points to under-filled cells until $n_j = N_{\text{threshold}}^{\text{p3}}$.

Figure 6(c) shows the property evaluation method p3. Density gradients are smoother and no artificial high-density cells remain.

The temperature of property method p3 is a weighted version of Eq. 17 using Eq. 13

$$T_{j,p3} = \frac{1}{n_j} \sum_{l=1}^{n_j} \frac{\sum_{i=1}^N T_{i,\text{SPH}} m_{i,\text{SPH}} W_{il}(r_{il}, h_i)}{\rho_{l,p1}}, \quad (18)$$

again $N > N_{\text{neighbor}}$ as in method p1.

When mapping the density with method p1, we recover a total mass of $7495 M_{\odot}$ extremely close to the actual mass of $7500 M_{\odot}$.

3.3.4. Results — Mapping

In Figure 6, we show different methods of mapping the SPH density and temperature onto the Voronoi mesh.

We found that kernel evaluation method p1 is efficient and reliable in small cells. The solving of the kernel function using the $N > N_{\text{neighbor}}$ nearest neighbors is sufficient to approximate the properties at the new position. But method p1 creates artifacts for large cells.

The splitting kernel method p2 is less computationally efficient but produces a smooth density or temperature gradient between large cells. For small cells this method breaks down, since the probability that a small cell gets "hit" by split particles is small. Therefore, the introduced threshold $N_{\text{threshold}}^{\text{p2}} = 10$ is important. For such small cells, we use the method p1. We found that a virtual splitting the SPH particle by $N_{\text{split}}^{\text{p2}} = 100$ produces a solid result while being tolerably efficient in time.

Method p3 removes the statistical sampling issues of the small cells (compared to method p2) by adding random sampling points within the cell as long as $N_{\text{threshold}}^{\text{p3}}$ is reached. We found that a smooth gradient in temperature or density can be reached when setting the number of points to sample to $N_{\text{random}} \approx 2 \times 10^7$ and the threshold to $N_{\text{threshold}}^{\text{p3}} = 20$. The trade-off is that this method is less efficient computationally when comparing with method p2, but it is fast enough for the purposes of our work.

¹² This method was developed by Francesco Biscani and Thomas Robitaille.

Below, we list the total mass within the simulation box of time-step 122 (6.109 Myr), recovered from the density mapping for every method present in this section:

$$m_{\text{p1}}^{\text{tot}} \approx 139\,945 M_{\odot} \quad (19)$$

$$m_{\text{p2}}^{\text{tot}} \approx 7530 M_{\odot} \quad (20)$$

$$m_{\text{p3}}^{\text{tot}} \approx 7495 M_{\odot} \quad (21)$$

The actual mass within the box of the SPH simulation $m_{\text{SPH}}^{\text{tot}} = 7500 M_{\odot}$ (c.f. Table 1). In respect of mass conservation, we note that method p1 is completely unreliable. The small overestimate of method p2 results from the threshold mechanism¹³. In method p2, when there are less than $N_{\text{threshold}}^{\text{p2}}$ split SPH particles in the cell, only the density at the position of the site is estimated. This leads to an over-prediction of the cell's density. For this reason, method p1 and method p2 are faulty by definition, since they introduce too high densities to certain cells. Therefore, we suggest method p3 when mapping SPH distributions onto a Voronoi tessellation, since this overestimation is reduced (error below 1%) by sampling more positions in small cells. In Figure 8 we show how well method p3 works in recovering a density gradient from the initial simulation. Blue points represent the simulated peak density of the SPH particles and the black points represent the p3 circumstellar sites. Figure 8 shows that the technique succeeds to recover the density structure over 2 orders of magnitude over less than 0.1 pc.

4. SOURCES

In HYPERION, we can set up spherical sources (e.g. stars) which emit photon packets. The parameters for spherical sources are the luminosity L_* , radius R_* and spectra $F_{\nu*}$.

4.1. Pre-main-sequence Stellar Evolutionary Models

Assuming we want to set up a source resembling a forming star in D14 SPH simulations with mass M_* and age t_{age} (see Eq. 3), we can calculate the stellar radius R_* and the stellar effective temperature T_{eff} by interpolating pre-main-sequence stellar evolutionary tracks. In Figure 7, we plot the pre-main-sequence tracks of Siess et al. (2000) for stellar masses between $0.1 M_{\odot} \leq M_* \leq 7.0 M_{\odot}$ and Bernasconi & Maeder (1996) for stellar masses between $9 M_{\odot} \leq M_* \leq 60 M_{\odot}$.

We interpolate R_* , T_{eff} and L_* from the stellar evolutionary tracks using 3-d natural neighbor interpolation (for more details, see Sibson 1981) of the discrete samples M_* and t_{age} . In the rare cases, when the stellar masses lie beyond the stellar evolutionary tracks of Bernasconi & Maeder (1996), we interpolate the main-sequence data from Appendix E of Carroll & Ostlie (1996) to infer the parameters.

4.2. Spectra

We use the stellar photosphere models from Castelli & Kurucz (2004) and Brott & Hauschildt (2005, Phoenix

¹³ The threshold for the methods p2 and p3 mean different things. A high threshold in p2 improves the gradient but also overestimates the mass, while in the p3, a higher threshold improves the mass conservation.

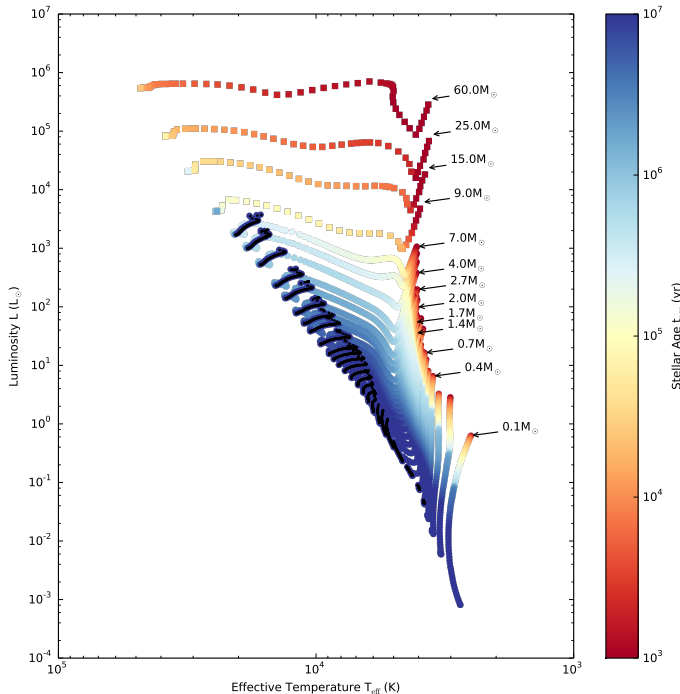


FIG. 7.— Luminosity versus effective temperature diagram of evolutionary pre-main-sequence tracks. Colors highlight stellar ages of the models. Arrows highlight the beginning of every mass track. Black points highlight stellar evolutionary phases, which have left the pre-main-sequence phase already.

models) to interpolate the spectra $F_{\nu,*}$ based on the parameters M_* , R_* and T_{eff} . The [Castelli & Kurucz \(2004\)](#) models are defined for stars with temperatures reaching from $3500 \text{ K} \leq T_{\text{eff}} \leq 50\,000 \text{ K}$, for logarithmic surface gravities

$$\log_{10} g_* = \log_{10} \left(\frac{GM_*}{R_*^2} \right). \quad (22)$$

between $\log_{10} g_* \in [0, 5]$ and for solar metallicities. In the rare cases when $T_{\text{eff}} < 3500 \text{ K}$, we use the Phoenix models. For a detailed description see [Appendix C](#).

5. CIRCUMSTELLAR MATERIAL

Now that we have mapped the density and temperature directly onto the Voronoi mesh (see [Section 3](#)) and that we have defined the stellar properties (see [Section 4](#)), it is possible to explore the regions around the accreting objects in more detail. Note that the circumstellar material is the most important place of the radiative transfer calculation, unfortunately unresolved below 1000 AU by the D14 SPH simulations. However, in the following, we describe several methods of how to overcome this and make sure that the density structure is as realistic as possible close to the sources.

5.1. Extrapolating the Envelope Density

As mentioned previously, the D14 SPH simulations are large-scale simulations and do not have as high resolution around the sink particles as other simulations of smaller scale. Even though the D14 SPH simulations lack the resolution to see the inner 0.01 pc close to the sink particles, we can already see a radial trend in the density close to accreting sink particles, which corresponds to the

outer regions of an envelope resolved by the SPH simulation (c.f. with the accreting sink particles 11640 and 110753 in [Figure 5](#)); in [Figure 8](#), we also replotted the sink particle 110753 to illustrate the following envelope refinement.

The blue colored points in [Figure 8](#) represent the SPH particles beyond the accretion radius $r_{\text{acc}} = 0.005 \text{ pc}$. We can see an accretion stream of SPH particles towards the sink particle 110753. But there is a gap of about 10^{-2} pc (cyan dashed) between the sink particle and the closest SPH particle. The envelope background density between the stream (outer envelope) and the sink particle is about $2 \times 10^{-19} \text{ g cm}^{-3}$ for object 110753. In [Section 3.2](#), we improved this situation by putting more circumstellar particles around the sink particle and evaluated their density in [Section 3.3](#) (see black points in [Figure 8](#)). The evaluated refined circumstellar density is somewhat only a background density of the outer envelope in the simulation and does not represent a continuous envelope with an increasing density profile at smaller scales. In [Figure 8](#), we can see the leveling off of the density profile for the new sites at $2 \times 10^{-19} \text{ g cm}^{-3}$ within the closest SPH particle of the accreting sink particles (black). In what follows, we extrapolate the envelope profile inwards with different profile descriptions. For the extrapolation, we will use the s3 circumstellar sites rather than the SPH particles close to the sink particles because we have better number statistics with the sites. We now describe three different methods for extrapolating the density structure to the smallest scales:

5.1.1. Method e1 — Ulrich Envelope Profiles

The Ulrich envelope profile ([Ulrich 1976](#)) is a rotational flattened profile and follows the physical process of accretion. The profile $\rho_{\text{Ulrich}}(r, \theta)$ is described in spherical coordinates and is dependent on the infall rate of material \dot{M}_{env} , the mass of the stellar object M_* and the centrifugal radius R_c :

$$\rho_{\text{Ulrich}}(r, \theta) = \rho_u^{\text{env}} \left(\frac{r}{R_c} \right)^{-3/2} \left(1 + \frac{\cos \theta}{\cos \theta_0} \right)^{-1/2} \times \left(\frac{\cos \theta}{\cos \theta_0} + \frac{2R_c \cos^2 \theta_0}{r} \right)^{-1} \quad (23)$$

$$\rho_u^{\text{env}} = \frac{\dot{M}_{\text{env}}}{4\pi(GM_*R_c^3)^{-1/2}}. \quad (24)$$

The angle θ_0 is given by the streamline equation:

$$0 = \cos^3 \theta_0 + \cos \theta_0 \left(\frac{r}{R_c} - 1 \right) - \cos \theta \left(\frac{r}{R_c} \right) \quad (25)$$

Hereafter, we call the Ulrich envelope profile¹⁴ method e1. We calculate the infall rate \dot{M}_{env} from the accretion rate (see [Eq. 5](#)). As can be seen in [Figure 8](#), we found that an Ulrich profile (left panel, purple lines) derived from the parameters of sink particle 110753 seamlessly

¹⁴ The Ulrich profiles are part of models in HYPERION, which sets up young stellar object (YSO) models from analytical density descriptions (see <http://www.hyperion-rt.org>). We will refer to these models in the remainder of this paper as Analytical YSO Models.

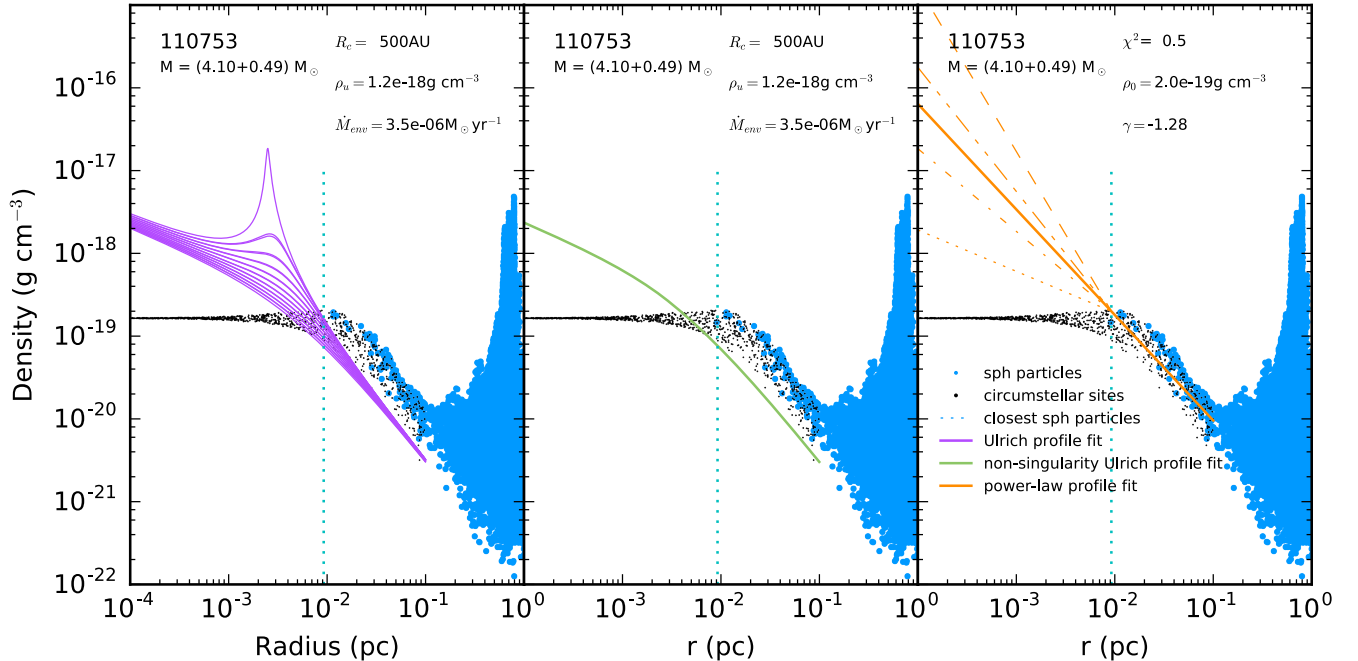


FIG. 8.— Radial density profile of SPH particles (blue) towards the sink particle 110753. The circumstellar sites of the accreting sink particle are over-plotted in black. (Left) rotationally flattened envelope fit (purple) at different angles, (middle) rotationally flattened envelope profile (green) with suppressed singularity at the mid-plane, (right) different power-law envelope profiles (dotted, dashed) and the fitted power-law profile (solid).

matches the accretion stream inwards but also underestimates it at larger radii. Note that the singularity at the centrifugal radius R_c (when $\cos \theta = \cos^3 \theta_0$; see Eq. 25) at the mid-plane (for $\theta = 90^\circ$; see Eq. 23) is caused by the pile-up of material as a result of angular momentum conservation. In reality, the material would be distributed radially to form a circumstellar disk.

5.1.2. Method e2 — Ulrich Envelope Profiles without Singularity

The Ulrich description of the circumstellar disk (i.e. the singularity) is not physically realistic. Therefore, for the density profile we ignore the singularity at the mid-plane and later add a more advanced description of the circumstellar disk in Section 5.4. In this method, hereafter named e2, we suppress¹⁵ the Ulrich singularity by adjusting the Ulrich density profile of Eq. 23:

$$\rho_{\text{Ulrich}}^{\text{no singularity}}(r, \theta) = \rho_u^{\text{env}} \left(\frac{r}{R_c} \right)^{-3/2} \left(1 + \frac{\cos \theta}{\cos \theta_0} \right)^{-1/2} \times \left(1 + 2 \frac{R_c}{r} \right)^{-1}. \quad (26)$$

In Figure 8 (middle), we present the rotationally flattened Ulrich profile with the singularity removed (green). We can see that the Ulrich distribution matches the sites at the inner rim of the envelope resolved by the SPH simulation, but underestimates the resolved SPH envelope profile at larger radii for object 110753.

5.1.3. Method e3 — Power-Law Envelope Profiles

As an alternative, and in order to understand how important the assumption of the envelope density profile

is for the final results, we also consider the case where we use envelopes with spherically-symmetric power-law profiles rather than the Ulrich collapse model (referred to as method e3). In the right panel of Figure 8, we show four different radial power-law profiles (diagonal dashed lines) with exponents $\gamma = [-0.5, -1.0, -1.5, -2.0]$ for the density function¹⁶

$$\rho(r) = \rho_0 (r/r_0)^\gamma. \quad (27)$$

The orange solid diagonal line is the log-scaled least-squares fit (Press et al. 1992) of the density distribution of the nearby SPH particles. The log-scaled least-square fit requires us to fit the following function:

$$\log_{10} \rho(r) = \log_{10} \rho_0 + \gamma \log_{10} (r/r_0). \quad (28)$$

For this accreting sink, the best fit of $\gamma = -1.25$ is a typical value for a protostar.

Note that a fitted power-law profile in density typically produces a better fit in terms of absolute scaling compared to the Ulrich profiles. However, spherical symmetric power-law density profiles with only one slope are not entirely physically motivated, whereas the Ulrich models are self-consistent with respect to the infall rate.

5.1.4. Results — Envelope Profiles

The Ulrich description (method e1) is a physically self-consistent envelope-infall model and is therefore consistent with the general physical picture, when improving the resolution on small scales by extrapolating inwards. However, the singularity at the centrifugal radius is unrealistic. Therefore, due to the singularity at the

¹⁵ Developed by Thomas Robitaille.

¹⁶ Power-law envelopes are part of the Analytical YSO Models in HYPERION as described on <http://www.hyperion-rt.org>.

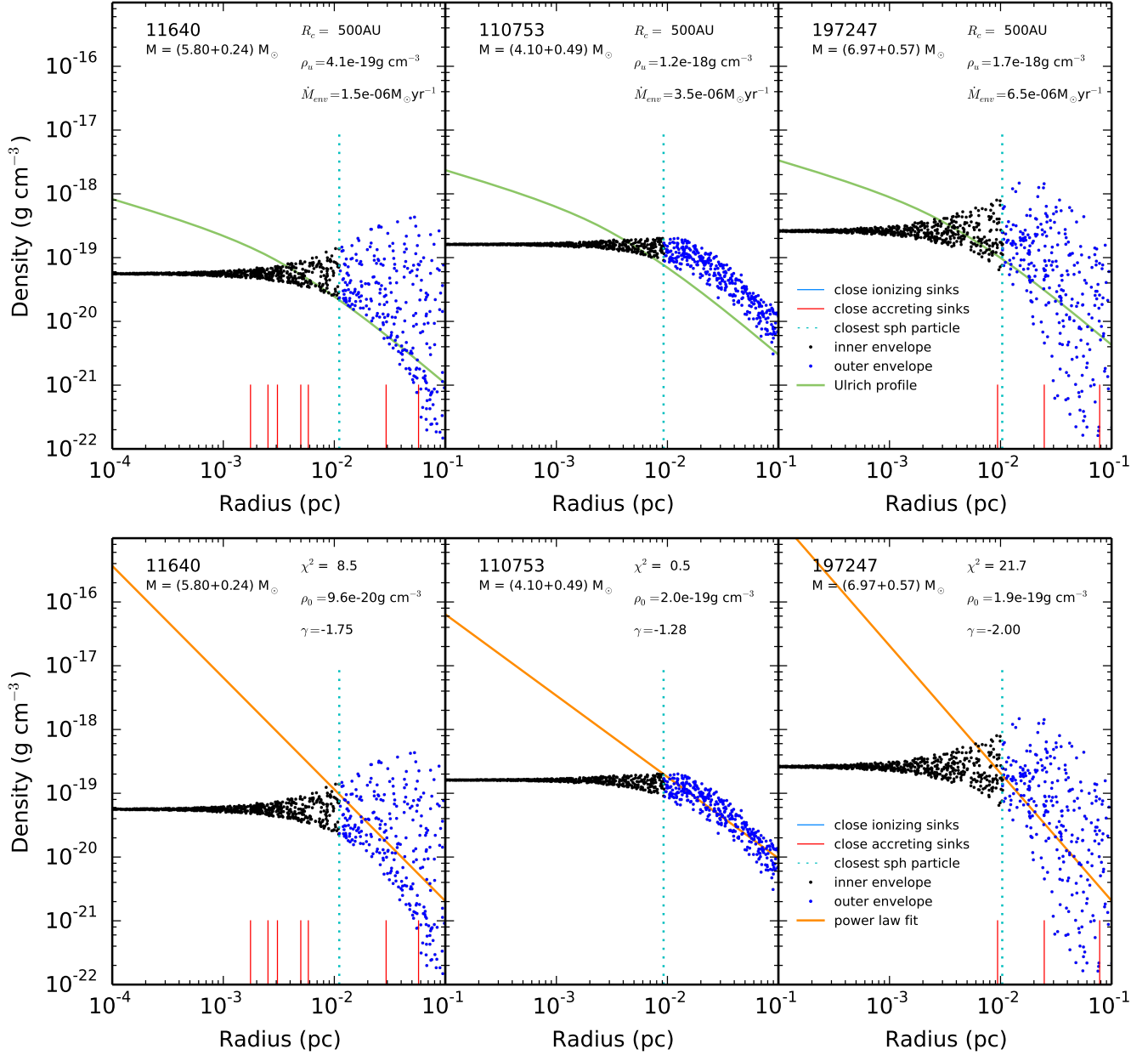


FIG. 9.— Radial density distribution of s3 sites and their envelope fits in time-step 122 (6.109 Myr). Red vertical lines highlight the distance of close accreting sink particles; cyan dotted lines show the distance of the closest SPH particle. (top) Green rotational flattened envelope profile: (a) for three relevant sink particles, (b - online material) for all relevant sink particles. (bottom) Orange lines plot the fit of the blue density sample of s3 sites: (a) for three relevant sink particles, (b - online material) for all relevant sink particles.

mid-plane, we do not use the standard Ulrich envelope (method e1).

However, we will use the Ulrich description without singularity e2 and add a circumstellar disk later in the radiative transfer set-up in Section 5.5. For the Ulrich description, we set the centrifugal radius R_c , hence the outer rim of the circumstellar disk, to $R_c = 500$ AU. The choice of the centrifugal radius is dependent on the chosen outer disk radius. 500 AU is a realistic intermediate value of typical values between 100 AU and 1000 AU. Moreover, the disk radius needs to be smaller than the accretion radius from the simulation ($r_{\text{acc}} = 0.005$ pc \approx 1000 AU), because otherwise the disk would have been resolved by the simulation. We calculate the density ρ_u^{env}

(see Eq. 23) for all Ulrich envelope fits. In Figure 9 (top panel), we show e2 rotationally flattened envelope profiles for the three accreting sink particles 11640, 110753 and 197247 with the corresponding values for ρ_u^{env} and \dot{M}_{env} . To see all profiles for time-step 122 (6.109 Myr) see the online extension of Figure 9 (top). While the majority of sink particle envelopes are reproduced well by Ulrich envelopes without singularities, this model underpredicts the density for some of the accreting objects. However, we cannot arbitrarily scale these particular profiles, because the mass M_* of the stellar object needs to drop for increasing ρ_u^{env} and constant infall rate \dot{M}_{env} (c.f. with Eq. 23).

The power-law method e3, which fits the envelope pro-

file, follows the slope of the radial profile of the outer envelope resolved by the SPH simulation, since it is an extrapolation of the gravitational collapse modeled in the D14 SPH simulations. We fit the slope of the profile γ and the density ρ_0 at the radius r_0 , which we set as the distance of the closest SPH particle. To extrapolate (see [Press et al. 1992](#)) the profile of the density for different cells j within $r_j < r_0$, we are only using s3 circumstellar sites of the outer envelope ($r_j > r_0$), which belong to the sink particles we want to fit the profile for. We only use sites from the outer envelope (see blue sample in [Figure 9](#)), since the inner density values (black) represent the background density of the outer envelope created by the SPH field close to the sink particle. In the bottom panel of [Figure 9](#), we show the power-law fits of the accreting sink particles 11640, 110753 and 197247 in time-step 122 (6.109 Myr), and we show the same for all accreting sink particles of this time-step in the online extension of [Figure 9](#) (bottom). We limit the slope of the profile to the range $\gamma \in [0, -2]$, because for $\gamma = 0$ the density follows the flat background density at the s3 circumstellar sites calculated in [Section 3.3](#). The limit $\gamma = -2$ was chosen because it corresponds to the radial profile of the "singular isothermal sphere" in gravitational collapse (see [Shu 1977](#)). From [Figure 9](#), we can see that the accretion stream (blue) is not spherically symmetric when the accreting sink particles sit in a close cluster of sink particles (11640, 197247) rather than being isolated (110753). We use a χ^2 value (see [Press et al. 1992](#)), to quantify the quality of the envelope profile fit:

$$\chi^2 = \sum_{j=1}^{N_j} \frac{(\log_{10} \rho(r_j) - \log_{10} \rho_{\text{fit}}(r_j))^2}{|\log_{10} \rho_{\text{fit}}(r_j)|}. \quad (29)$$

We need N_j , which are all the sites that belong to the refined circumstellar sites of a sink particle with $r_j > r_0$, and $\rho_{\text{fit}}(r_j)$, which is [Eq. 28](#) evaluated for the fitted parameters γ_{fit} , and $\rho_{0,\text{fit}}$ to calculate

$$\log_{10} \rho_{\text{fit}} = \log_{10} \rho_{0,\text{fit}} + \gamma_{\text{fit}} \log_{10}(r_j/r_0). \quad (30)$$

Spherically symmetric profiles produce a better fit and have lower χ^2 values, as can be seen in the bottom panel of [Figure 9](#). However, when comparing with method e2, which uses the rotational flattened envelope profile without singularity, we see that in the central region, the power-law density is several orders of magnitude higher.

While the Ulrich profile is consistent with the physical picture of a gravitational collapse with conservation of angular momentum, the gravitational collapse description in the D14 SPH simulations should reproduce power-law profiles on small scales. The power-law profiles in the D14 SPH simulations are limited by the isothermal accretion flow of $\rho \sim r^{-2}$ at larger radii ($r > 0.1$ pc). Additionally, within the accelerating collapsing shell ($r < 0.1$ pc), the velocity is not constant and the density profile is shallower, with $\rho \sim r^{-3/2}$ ([Shu 1977](#); [Ulrich 1976](#)). This explains the offset of the radial density profile of the outer envelope from the simulations, compared to the rotationally flattened envelope profile and why the power-law profiles produces a better fit. Although the power-law profiles are consistent with the gravitational collapse description used in the D14 SPH simulations, the rotational flattened envelope

profiles are consistent with the physical picture of small scale gravitational collapse.

To explore the effects of the choice of refinement techniques on the synthetic observations, we will provide the results for both methods e2 and e3 in this paper.

5.2. Envelope Superposition

In some cases, the accreting sink particles lie in compact clusters that include other accreting sink particles. As a result, the different envelope profiles will overlap, increasing the density further. An overlap means different things for the two different envelope descriptions e2 and e3. In the self-consistent picture of an infalling envelope (e2: Ulrich profile), the overlap is represented by summation, since the infalling mass is increasing. For the power-law envelope description (e3), the maximum of the superimposed envelopes at every position is the resulting envelope profile, since if the envelopes of two sink particles with the same power-law would overlap, the resulting fit would again be the initial power-law envelope, and not a power-law envelope twice as dense.

By using a smooth weighting function, we combine the density of the envelope and the background and recover a smooth transition between the two. Additionally, for sink particles that are close to other sink particles, we then also weight the density of the different envelopes accordingly, before evaluating a final density at each point. We describe these two cases in the next two sections.

5.2.1. Weighting

We calculate the distance r_{js} , envelope density ρ_{js}^{env} of every s3 circumstellar site j and every accreting sink particle s for which we have already calculated the "background" density of method p3 $\rho_{p3,j}$ in [Section 3.3](#). We define that an envelope of a sink particle only contributes when $r_{js} < r_{\text{max}}$, where r_{max} is the maximum distribution radius of s3 circumstellar sites that belong to a sink particle as described in [Section 3.2](#), otherwise we set all elements of $\rho_{js}^{\text{env}} = 0$. We weight ([Press et al. 1992](#)) the density ρ_{js}^{env} by:

$$w_{j,s} = \begin{cases} 1 & \forall r_{js} < r_{0,s} \\ 1 - \frac{r_{js} - r_{0,s}}{r_{\text{max}} - r_{0,s}} & \forall r_{0,s} \leq r_{js} \leq r_{\text{max}} \\ 0 & \forall r_{js} > r_{\text{max}} \end{cases} \quad (31)$$

where $r_{0,s}$ is the radius of the closest sink particle, as described in [Section 5.1](#). The "background" density $\rho_{p3,j}$ is weighted with the counter weight

$$\tilde{w}_{j,s} = 1 - w_{j,s}. \quad (32)$$

We set all weights $w_{j,s}$ and $\tilde{w}_{j,s}$ to zero when the density $\rho_{js}^{\text{env}} = 0$.

5.2.2. Weighted Superposition

For the Ulrich description of method e2 we sum the weighted density function to get the superposition envelope density $\hat{\rho}_{j,p3}$ at every site j with

$$\hat{\rho}_{j,p3}^{\text{e2}} = \sum_{s=1}^{N_s} \left[w_{j,s} \rho_{js}^{\text{env}} + \rho_{p3,j} \tilde{w}_{j,s} \right], \quad (33)$$

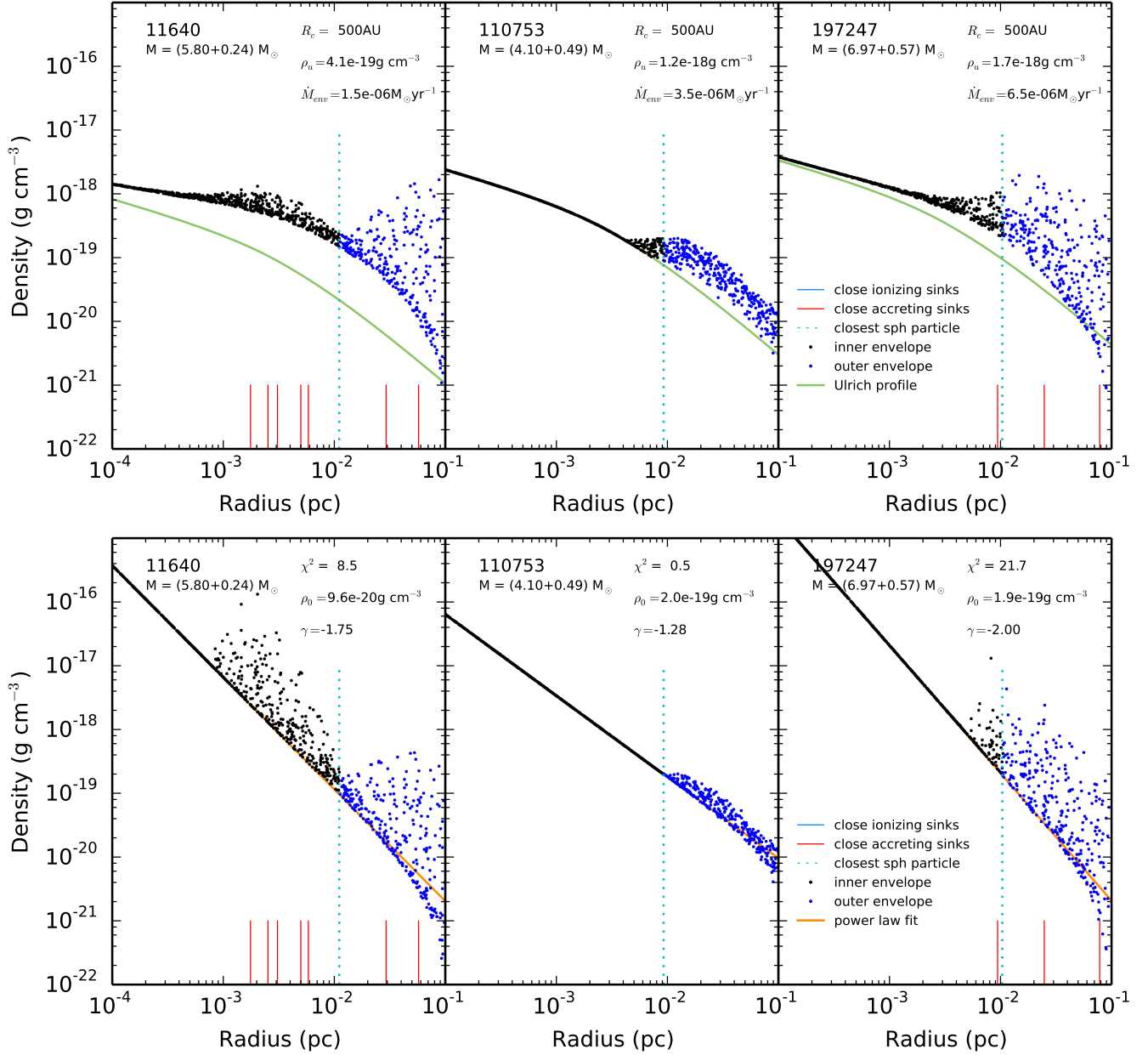


FIG. 10.— Extrapolated envelope density distribution of s3 sites including superposition and their envelope profiles in time-step 122 (6.109 Myr). Red vertical lines highlight the distance of close accreting sink particles; cyan dotted lines show the distance of the closest SPH particle. (top) Green rotational flattened envelope profile: (a) for three relevant sink particles, (b - online material) for all relevant sink particles. (bottom) Orange lines plot the fit of the blue density sample of s3 sites. (a) for three relevant sink particles, (b - online material) for all relevant sink particles.

by using the normalization N_s , which is the number of accreting sink particles with envelopes. The summation is necessary, since the Ulrich envelope was constructed from the physical parameters, such as the infall rate \dot{M}_{env} .

As explained above, for the power-law description e3, we take the maximum of the weighted density function when superimposing many envelopes

$$\hat{\rho}_{j,p3}^{\text{e3}} = \max_{s=1}^{N_s} \left[w_{j,s} \rho_{js}^{\text{env}} + \rho_{p3,j} \tilde{w}_{j,s} \right]. \quad (34)$$

When the superposition density is lower than the background density $\rho_{p3,j}$, for example in some cases the outer regions of the Ulrich envelope fits are too low,

we set $\hat{\rho}_{j,p3} = \rho_{p3,j}$. In Figure 10, we show the inward-extrapolated densities of the envelope profiles including superposition. For all objects in time-step 122 (6.109 Myr), see the online extension of Figure 10. For the isolated object 110753, we only see the density extrapolation inwards, while for the object 11640 and 197247 we see a superposition. For instance, in the upper panel in Figure 10, where we show the Ulrich description of method e2, we can see that for the non-isolated objects 11640 and 197247, the new profile is higher than the initial fit (green) with values approaching the initial fit at small radii.

For the power-law envelope of method e3 in the lower

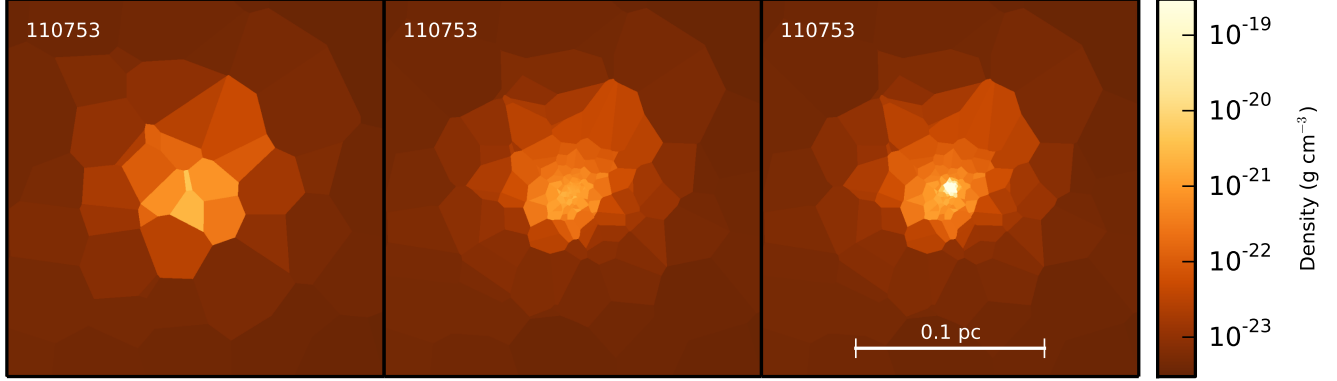


FIG. 11.— Different methods of envelope profiles for the sink particle 110753 in *run I* step 122 (6.109 Myr). Region around the sink particle with site method s1 (left); region around the sink particle with site method s3 (middle); region around the sink particle with site method s3 and added envelope profile (right).

panel of Figure 10, this effect was suppressed due to the fact that we take the maximum of the envelope densities rather than the sum, as shown in Eq. 34. We can see that there is a smooth transition to other envelopes (black particles in object 11640 and 197247) and also a seamless transition¹⁷ to the radial profile of other envelopes resolved by the SPH simulation (blue particles).

In Figure 11, we present a 2-d slice through the density structure in order to show the improvement in resolution for the accreting sink particle 110753. The left panel shows the density evaluated on the grid where each cell corresponds to an SPH particle (s1), the central panel shows the improvement once the circumstellar cells are added (s3), and finally the panel on the right shows an inward extension of the envelope including the superposition of envelope densities $\hat{\rho}_{j,p3}$ for a rotationally flattened envelope (e2).

5.3. Envelope Cavities

YSOs drive outflows that carve out bipolar cavities in the envelopes, mostly perpendicular to the mid-plane (for more details, see Whitney et al. 2003). We parameterize the outflow cavity walls¹⁸ as:

$$z(r) = \pm ar^{3/2}. \quad (35)$$

We choose the opening constant a in such a way that at the outer radius of the envelope R_{max}^{env} , the half-opening angle θ_{open} is equal to $\theta_{open} = 10^\circ$:

$$a = R_{max}^{env} \cos(\theta_{open}). \quad (36)$$

We assume that the material in the cavity is optically thin so that the radiation can escape. Therefore, we set the cavity density

$$\rho_{cavity} = 0. \quad (37)$$

The cavity removes a certain fraction from the total mass. For the rotational flattened envelopes (e2) about

¹⁷ Note that superimposed envelopes close to ionization bubbles could now create large high-density cells in the outer rim of the circumstellar sites for an individual accreting sink particle. To avoid this, we set in those cases (cell volume larger than 5% of the envelope volume at the certain radius) the superimposed density to the background density of the cell $\rho_{j,p3}$ before superposition and envelope extrapolation.

¹⁸ The description follows the Analytical YSO Models in HYPERION as described on <http://www.hyperion-rt.org>.

2% is removed, while for the power-law envelope (e3) up to 4% is removed.

5.4. Circumstellar Disks

In the last three sections, we focused on the envelope of accreting stellar objects in the D14 SPH simulations. Physically, on smaller scales, the accreting material of the envelope is channeled through the disk to the central object. From the D14 SPH simulations, we extracted the total angular momentum vector \mathcal{L}_{tot} of the accreting sink particles to determine the inclination $\Delta\theta$ of all disks in the simulation at every time-step:

$$\mathcal{L}_{tot} = \sqrt{\mathcal{L}_x^2 + \mathcal{L}_y^2 + \mathcal{L}_z^2} \quad (38)$$

$$\Delta\theta = \arccos(\mathcal{L}_z/\mathcal{L}_{tot}) \quad (39)$$

We can evaluate the density contributed by the disk $\rho_{disk}(r, \theta)$ for the s3 circumstellar sites of a sink particle at a certain radius r and at an angle θ (see Eq. 11) through the flared disk¹⁹ (Armitage 2010) density profile (e.g. Whitney et al. 2003; Shakura & Sunyaev 1973) below. By replacing θ by $\theta - \Delta\theta$, we incline the disk, as set by the angular momentum vector (see Eq. 38 and Eq. 39):

$$\rho_{disk}(r, \theta) = \begin{cases} \rho_{disk} \forall r_{min}^d < r \leq r_{max}^d, \\ 0 \quad \forall r > r_{max}^d \end{cases} \quad (40)$$

$$\rho_{disk} = \rho_{norm} \left(\frac{r_0}{r}\right)^{\beta-p} \exp\left[-\left(\frac{r \cos(\theta - \Delta\theta)}{4h}\right)^2\right] \quad (41)$$

with the disk flaring parameter β , the surface density exponent p , the maximum disk radius r_{max}^d , the minimum disk radius r_{min}^d and disk scale height h , which is defined as a relation of the height h_0 at radius r_0 :

$$h = h_0 \left(\frac{r}{r_0}\right)^\beta. \quad (42)$$

The integration normalization constant ρ_{norm} is defined to satisfy that the volume integral of the disk density

¹⁹ The description follows the Analytical YSO Models in HYPERION as described on <http://www.hyperion-rt.org>.

function of Eq. 40 is equal to the disk mass:

$$M_{\text{disk}} = \int_0^{2\pi} d\phi \int_{-\pi}^{\pi} d\theta \int_0^{r_{\text{max}}^d} dr r^2 \sin\theta \rho_{\text{disk}}(r, \theta) \quad (43)$$

which can be solved numerically. Since we assume the mass of the disk $M_{\text{disk}} \approx 10^{-2} M_*$, we can solve, with the help of Eq. 40 for ρ_{norm} . We calculate the disk density distribution $\rho_{\text{disk}}(r, \theta, j)$ for all the s3 circumstellar sites j with the following values:

$$M_{\text{disk}} = 10^{-2} M_* \quad (44)$$

$$r_0 = 1000 \text{ AU} \quad (45)$$

$$h_0 = 50 \text{ AU} \quad (46)$$

$$r_{\text{min}}^d = r_{\text{OptThin}}(T_{\text{dust}} = 1600 \text{ K}) \quad (47)$$

$$r_{\text{max}}^d = R_c = 500 \text{ AU} \quad (48)$$

$$\alpha = -1.0 \quad (49)$$

$$\beta = 1.25 \quad (50)$$

where $r_{\text{OptThin}}(T_{\text{dust}} = 1600 \text{ K})$ is the sublimation radius²⁰, given by the radius at which the temperature would drop to 1600K in an optically-thin medium:

$$r_{\text{OptThin}}(T_{\text{dust}}) = R_* \left[1 - \left(1 - 2 \frac{T_{\text{dust}}^4}{T_{\text{eff}}^4} \frac{\kappa_B(T_{\text{dust}})}{\kappa_*} \right)^2 \right]^{-1/2} \quad (51)$$

where κ_B is the Planck mean opacity, κ_* is the mean opacity of the dust weighted by the stellar photosphere and T_{eff} is the effective temperature of the star. Note that when dust properties, including polycyclic aromatic hydrocarbon (PAH) molecules, are used, we set the inner radius to $r_{\text{OptThin}}(T_{\text{dust}})$ for the largest dust grain.

5.5. Circumstellar Set-up

In Section 3, we discussed different methods for how to distribute sites and how to evaluate the density and temperature when transferring from a particle-based SPH simulation to a Voronoi tessellation. With a description of the temperature T_{p3} and the "background" density ρ_{p3} , we described how to evaluate the properties of the stellar sources in Section 4. Further, the circumstellar density can be computed by using the envelope profiles e2 and e3 (see Section 5.1) in order to evaluate the overlapping envelope density $\hat{\rho}_{\text{p3}}$ (see Section 5.2). We described the bipolar outflow cavity set-up in Section 5.3. For smaller scales the disk density ρ_{disk} (Section 5.4) can contribute at s3 circumstellar sites close to the accreting sink particle.

In this section, we will combine the above prescriptions and explore three different approaches of setting up the circumstellar material from the radiative transfer calculation. In Figure 12, we plot sketches of the different methods of the circumstellar material set-up and summarize the different configuration in Table 2.

5.5.1. Method CM1 — No Circumstellar Matter

The simplest approach (hereafter, CM1), is not to add any circumstellar material on top of the density given by

²⁰ Description from <http://www.hyperion-rt.org> and derived by Thomas Robitaille.

the SPH simulation, but still include circumstellar sites to ensure that the temperature profile around the sources is resolved. The radiative transfer calculation is then set up as listed in Table 2.

5.5.2. Method CM2 — e2 Envelope, Cavity & Disk from "Analytical YSO Models"

We extend the first approach by using the densities from the rotationally flattened envelopes (e2), we evaluated in Section 5.1, and also account for their superposition (see Section 5.2) and hereafter call this circumstellar material method, method CM2. We used the superimposed density $\hat{\rho}_{j,\text{p3}}$ for sites of accreting sink particles, however we set the superimposed envelope density $\hat{\rho}_{j,\text{p3}}$ of sites j within the disk radius $r_j < r_{\text{max}}^d = 500 \text{ AU}$ (as defined in Eq. 48) to zero and rather include an Analytical YSO Model in the center. For illustration, see Figure 14 (middle).

For the inner 500 AU, we set up the Analytical YSO Model using the radiative transfer code HYPERION, which is adding the spectral energy distribution (SED) of the YSO (star, envelope, cavity & disk).

With the higher density material present, we need to adjust the mass of the source in the radiative transfer by the mass of the added circumstellar material (envelope, cavity, disk) between r_0 and $r_{\text{min}} \approx 0$. Therefore, we calculate the envelope mass $M_{\text{env}}^{\text{e2}}$ by numerically integrating over the envelope density profile. We use the bi-polar cavity set-up described in Section 5.3 and set the outer radius of the envelope in the cavity description (Eq. 36) to $R_{\text{max}}^{\text{env}} = 500 \text{ AU}$. The cavity removes about 2% from the mass of the envelope within $R_{\text{max}}^{\text{env}}$. We scale the disk density ρ_{disk} thus that the disk mass M_{disk} (from Eq. 43) is 1% of the stellar mass M_* . The other parameters of the Analytical YSO Models are set up with the parameters given in Section 5.4. The new mass of the stellar particle is then calculated as follows:

$$M_* = M_{\text{sink}} - (M_{\text{env}}^{\text{e2}} - M_{\text{cavity}}^{\text{e2}}) - M_{\text{disk}}. \quad (52)$$

The method CM2 sets up with the parameters listed in Table 2. We use this set-up to precompute the SED of the Analytical YSO Model. Since the Analytical YSO Model is not spherically symmetric, we compute the models for different viewing angles and determine an angle-averaged SED that we then use in the radiative transfer calculation. Therefore, we average the computed SED over 12 isotropically spaced viewing angles.

5.5.3. Method CM3 — e3 Envelope, Cavity & Disk from Analytical YSO Models

Method CM3 is similar to CM2 but with power-law envelopes instead of rotationally flattened Ulrich envelopes. The envelope mass $M_{\text{env}}^{\text{e3}}$ can be, therefore, calculated analytically as the spherical volume integral of the density

TABLE 2
SUMMARY OF SET-UPS FOR DIFFERENT CIRCUMSTELLAR CONFIGURATIONS.

method	CM1	CM2	CM3
envelope fitting	-	e2	e3
sites	s3	s3	s3
density	ρ_{p3}	$\hat{\rho}_{j,p3}^{e2}(r_{j,s} > r_{max}^d)$	$\hat{\rho}_{j,p3}^{e3}(r_{j,s} > r_{max}^d)$
density reference	Eq. 17	Eq. 34	Eq. 34
Analytical YSO Model	no	yes	yes
source mass	$M_* = M_{\text{sink}}$	$M_* = M_{\text{sink}} - (M_{\text{env}}^{e2} - M_{\text{cavity}}^{e2}) - M_{\text{disk}}$	$M_* = M_{\text{sink}} - (M_{\text{env}}^{e3} - M_{\text{cavity}}^{e3}) - M_{\text{disk}}$
mass references	D14 SPH simulations	Eq. 43	Eq. 53, 43

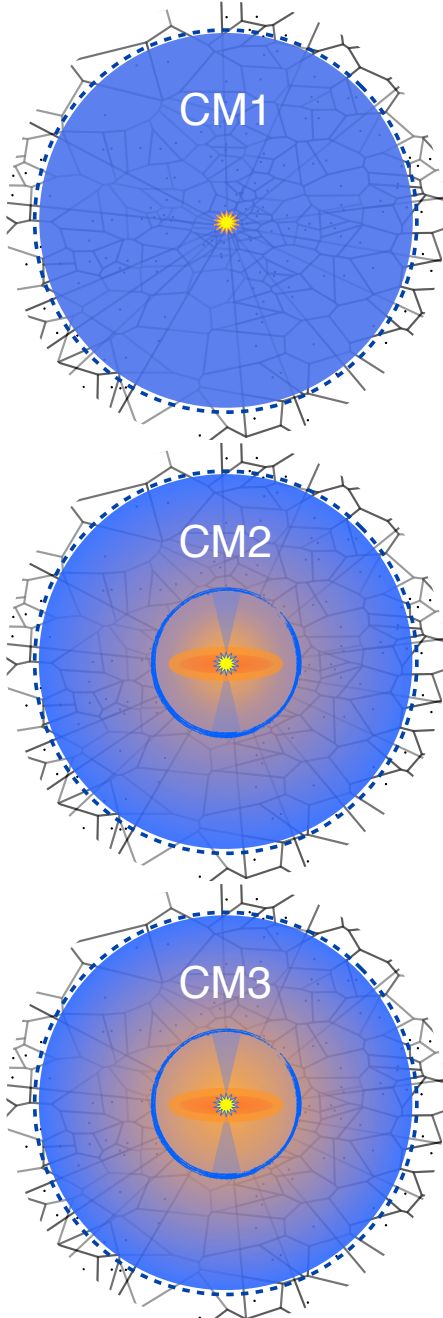


FIG. 12.— Three methods of circumstellar material set-up in the radiative transfer calculations.

function from Eq. 27 between r_0 and $r_{min} \approx 0$.

$$M_{\text{env}}^{e3} = \int_0^{2\pi} d\phi \int_{-\pi}^{\pi} d\theta \int_{r_{min}}^{r_0} dr r^2 \sin\theta \rho(r) \quad (53)$$

$$= 4\pi\rho_0 \int_{r_{min} \approx 0}^{r_0} dr \left(\frac{r}{r_0}\right)^\gamma r^2 \quad (54)$$

$$\approx \frac{4\pi}{\gamma+3} \rho_0 r_0^3 \quad (55)$$

In Table 2, we summarize the set-up parameters of method CM3. Note that the cavity removes about 4% from the mass of the envelope within R_{max}^{env} .

5.5.4. Results — Circumstellar Material Set-up

Above we presented the circumstellar material set-up versions CM1 (star alone), CM2 (star & e2 Analytical YSO Models) and CM3 (star & e3 Analytical YSO Models).

Method CM1 is the simplest approach when setting up a radiative transfer model from simulations, because it does not require an inward envelope extrapolation. For instance, [Offner et al. \(2012\)](#) used this approach without circumstellar refinement because the circumstellar material was too optically thick to contribute to the flux that they were interested in.

However, in this work we will present a parameter study: From now on we will use method CM1, CM2 and CM3 to set up the circumstellar material in the radiative transfer set-up and therefore explore the effects of circumstellar material on the MIR flux.

6. DUST & TEMPERATURES

Now that the density has been successfully mapped onto the radiative transfer grid and stellar sources including the circumstellar material have been set up, we will focus in this section on the dust and the temperature set-up.

6.1. Dust Properties

We set the dust-to-gas ratio to a typical value of $\frac{\text{dust}}{\text{gas}} = 0.01$ ([Draine 2011](#)). When computing the radiative transfer, we explore two different sets of dust properties:

- one that assumes thermal emission for all grain sizes ([Draine 2003](#); [Weingartner & Draine 2001](#)) and

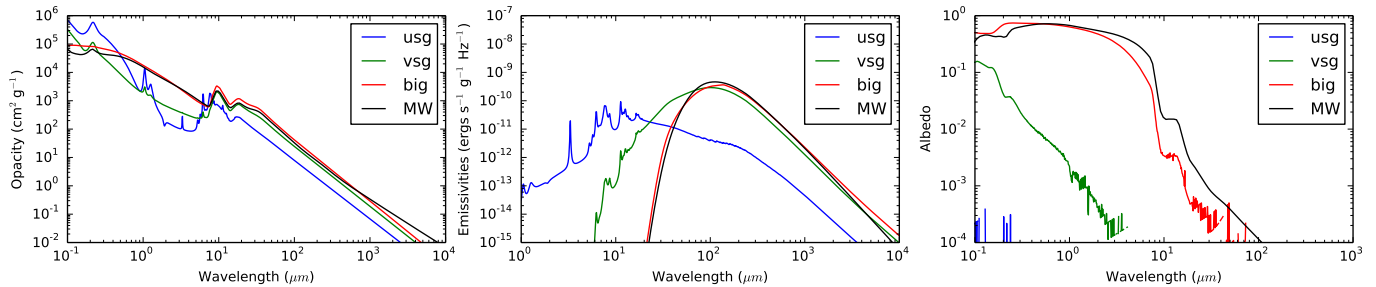


FIG. 13.— Dust opacity, emissivity and albedo of the ultra-small (usg), very small (vsg) and big grains (big) of the PAH dust models and the non-PAH Milky Way dust (MW). Note that the panels have a different scale in wavelength.

- one that also takes into account the transient heating of very small grains and PAH molecules (Draine & Li 2007).

We will refer to these as non-PAH dust and PAH dust respectively. In Figure 13, we show the opacity, emissivity and albedo of the different dust components.

6.1.1. Non-PAH Dust

In Figure 13, we show the properties of the Milky Way non-PAH dust from Weingartner & Draine (2001) with the re-normalization of abundances from Draine (2003) with $R_V = 5.5$ and $b_c = 3.0$, where R_V is the ratio of the visual extinction to reddening magnitude, and b_c is the concentration of carbon atoms in the medium. These dust properties reproduce the fluxes of the far-infrared (FIR) well but lacks emission in the near-infrared (NIR) and MIR up to 20 μm .

6.1.2. PAH Dust

We use an approximate method for the treatment of the emission from dust grains and PAH molecules, following Robitaille et al. (2012, and private communication with Bruce Draine therein). We separate the dust size distribution into three grain species: 80.63% big grains ($>200 \text{ \AA}$); 13.51% of a smaller dust species within 200 \AA and 20 \AA , called very small grains (vsg); and 5.86% of the PAH molecules, called ultra-small grains ($<20 \text{ \AA}$, usg).

The very small and ultra-small grains are transiently heated as mentioned above, while the big grains are in local thermodynamical equilibrium (LTE), similarly to the non-PAH dust. When comparing the non-PAH dust (black) with the big grains (red) in Figure 13, we can see that the opacities are not that different, while the ultra-small grains (blue) and very small grains (green) have pronounced features in the MIR. The strong emissivity values of the ultra-small grains below 20 μm causes the PAH emission typically observed towards high-mass star-forming regions.

6.2. Temperature Combinations

In HYPERION, it is possible to couple the calculated radiative transfer temperature of the dust $T_{\text{RT}}^{\text{dust}}$ to the hydrodynamical temperature mapped onto the Voronoi mesh $T_{\text{p}3}$. We will now explore the effects for different dust types and temperature combinations:

6.2.1. Method DT1

The method DT1 combines the radiative transfer temperature $T_{\text{RT}}^{\text{dust}}$, calculated from the non-PAH and PAH

dust with the hydrodynamical temperature $T_{\text{p}3}$.

$$T_{\text{RT}}^{\text{tot}} : T_{\text{RT}}^{\text{dust}} \ \& \ T_{\text{p}3} \quad (56)$$

Note that for the PAH dust only the big grains can heat thermally, and therefore, we couple only big grains with the hydrodynamical temperature. The temperatures are not directly summed, since this would not be physical. In HYPERION, the temperature is actually represented by the specific energy rate $\dot{\epsilon}$ (changes in absorption and emission process), which under the assumption of LTE can be transferred into a corresponding temperature. Therefore, the temperatures can be combined by converting them to $\dot{\epsilon}(T)$, and adding those energies before they are converted back.

6.2.2. Method DT2

We will further explore the effects when coupling $T_{\text{RT}}^{\text{dust}}$ with an isothermal temperature $T_{\text{iso}} = 18 \text{ K}$ for the two different dust types in method DT2. The constant temperature of 18 K on average matches the temperature in relatively empty patches in the Galactic plane (see Paper II for more details), and is therefore a good choice for an ambient temperature.

$$T_{\text{RT}}^{\text{tot}} : T_{\text{RT}}^{\text{dust}} \ \& \ T_{\text{iso}} \quad (57)$$

Note that for the PAH dust, the temperature is only significant for the big grains, which satisfies LTE. Therefore, we couple only big grains with the isothermal temperature.

6.2.3. Method DT3

In the method DT3, as a sanity check, we only run the radiative transfer without combining with an extra temperature.

$$T_{\text{RT}}^{\text{tot}} : T_{\text{RT}}^{\text{dust}} \quad (58)$$

6.2.4. Results — Dust & Temperature Combinations

We produce ideal synthetic observations of the methods DT1, DT2 and DT3 using non-PAH and PAH dust at 20 μm and present them in Figure 14, where we also show a background subtracted image at WISE 22 μm of the Soul Nebula (Koenig et al. 2012; Wright et al. 2010), a real star-forming region, in the right panel.

We now focus on the non-PAH dust in the upper panels of Figure 14. We note that the non-PAH dust produces much too bright emission²¹ in comparison to the

²¹ Note that the white pixels at the rim of the set-up DT1 are more than 10 \times brighter than the maximum value in the W5 panel. Therefore, also the total flux of the DT1 set-up is much higher than other comparable values.

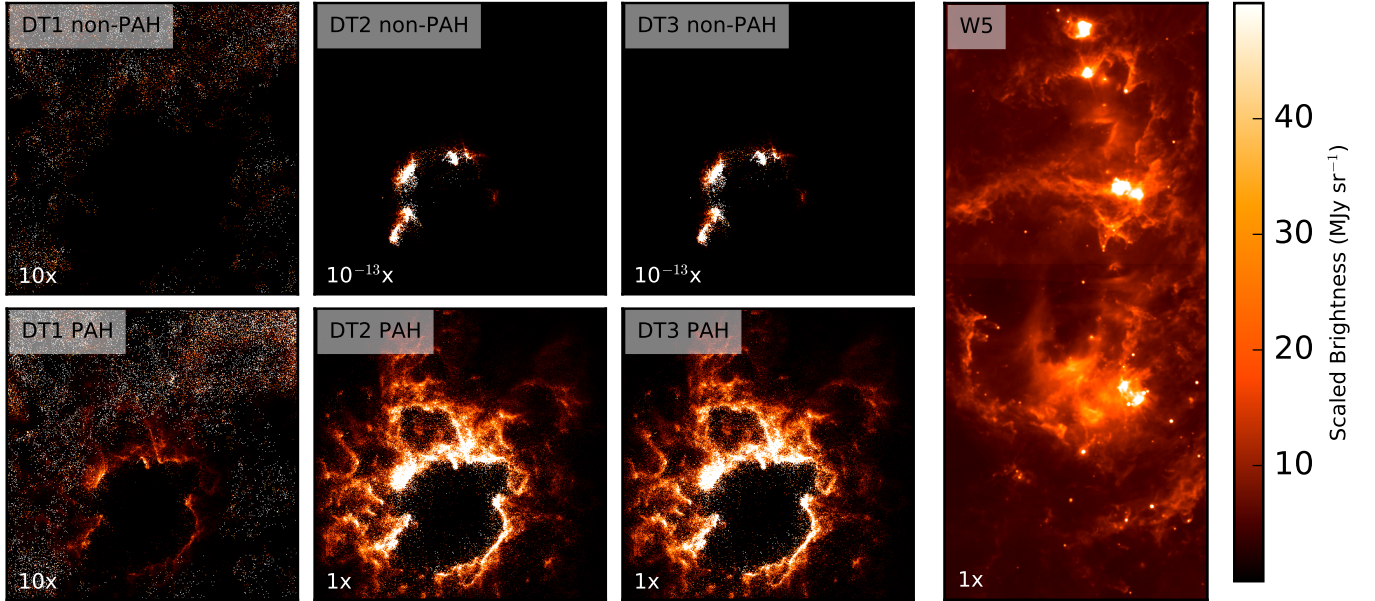


FIG. 14.— Ideal synthetic observations for different temperature combinations and dust types. The right panel shows the background subtracted image at WISE 22 μm of the Soul Nebula (c. f. with Figure 1), a real star-forming region. Note that the images do not all have the same color scaling. The white numbers in the individual panels represent the scaling factors of the images in respect to the colorbar. A low scaling factor stands for low brightnesses.

real region, when coupling with the hydrodynamical temperature (see method DT1). The coupling of isothermal and radiative transfer temperature (DT2) produces drastically too low brightnesses (note the colorbar scaling factor 10^{-13}) as does the radiative transfer temperature alone (DT3).

We found that the PAH dust in the lower panels of Figure 14 can reproduce the typical surface brightness of the Galactic star-forming region better. While the coupling with the hydrodynamical temperatures (see method DT1) causes even higher brightnesses than its non-PAH dust counterpart, neglecting the hydrodynamical temperatures produces better results: When combining the radiative transfer temperature with an ambient isothermal temperature (DT2), the brightness of the object is consistent with real observed regions. Also method DT3 produces a comparable result to the real star-forming region but lacks emission in the outer regions for longer wavelengths.

From Figure 14, we can see that when combining the radiative transfer temperature with the hydrodynamical temperature (see method DT1), the brightness in the MIR is overestimated for non-PAH and PAH dust. The high brightness components are produced by the high hydrodynamical temperatures T_{p3} in the outer regions, which was coupled with the dust radiative transfer temperature in Eq. 56. The gas temperatures are highest in the low density regions, due to the Larson (2005) EOS (c. f. Figure 2 and Section 2.2), but this is not observed for real star-forming regions. Although the temperatures of neutral SPH particles lie below the dust sublimation temperature of 1600 K (see Section 5.4), the brightness due to the hydrodynamical temperature is several orders too high, due to the erroneous assumption that the gas and dust are well-thermally coupled everywhere. In fact, the heating of the gas at low densities due to the Larson (2005) EOS used in the D14 SPH simulations, is phys-

ically due to the decoupling of the dust from the gas and therefore it does not make sense to use these high temperatures for the dust. Therefore, having explored the different ways of setting up the radiative transfer temperatures, we recommend using method DT2 by coupling the radiative transfer temperature $T_{\text{RT}}^{\text{dust}}$ with the ambient isothermal temperature T_{iso} for big grains of the PAH dust, which recovers the brightness features in the MIR much better.

7. REALISTIC SYNTHETIC OBSERVATIONS

In Paper II and Paper III, we will test and calibrate techniques commonly used by observers to infer star-formation properties. For this task, it is critical that we have synthetic observations which are as realistic as possible. We set up HYPERION with the preferred methods described from Section 2 to Section 6 and produce ideal synthetic observations. We then simulate all the effects introduced by telescopes and the Galactic environment with the FLUXCOMPENSATOR (Koepferl & Robitaille, in preparation, hereafter referred to FLUXCOMPENSATOR Paper). In the following sections, we will give a brief description of these simulated effects by the FLUXCOMPENSATOR.

7.1. Imaging

After the total temperature $T_{\text{RT}}^{\text{tot}}$ calculation/combination in HYPERION, the images are produced by the ray-tracing algorithm (Robitaille 2011). Note that for computational reasons we are not computing the scattering: For all the dust properties that we use, the albedo has values smaller than 1% above 8 μm (compare with Figure 13) and therefore, scattering is not important in the wavelength regimes we are interested in.

We produce ideal synthetic observations for 3 viewing angles looking down the x, y, and z axes respectively. We compute the ideal synthetic observations in a spectral

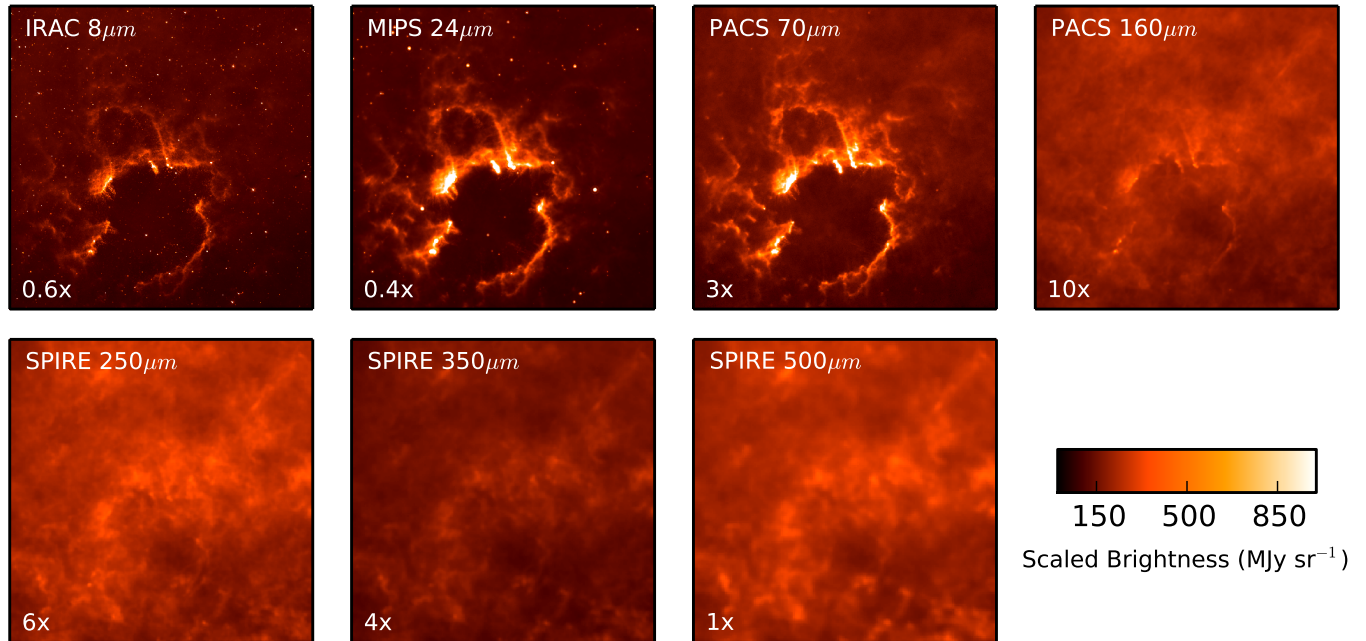


FIG. 15.— Realistic synthetic observations of a star-forming region of the D14 SPH simulations in Infrared Array Camera (IRAC) 8 μm , Multiband Imaging Photometer for *Spitzer* (MIPS) 24 μm , Photoconductor Array Camera and Spectrometer (PACS) 70 μm , PACS 160 μm , Spectral and Photometric Imaging Receiver (SPIRE) 250 μm , SPIRE 350 μm and SPIRE 500 μm combined with a real background of time-step 122 (6.109 Myr). Note that not all images have the same scale. The white numbers in the individual panels represent the scaling factors with respect to the colorbar.

cube of 30 steps in wavelength from 1 μm to 750 μm . The 2-d image slices of the cube span 1200×1200 pixels.

7.2. Distance

We push the ideal synthetic observations from HYPERION to a distance of $d = 3$ kpc to be roughly comparable to close high-mass star-forming regions, such as the Carina Nebula, the Eagle Nebula or the Heart and Soul Nebulae (Westerhout 4 & 5), and $d = 10$ kpc to represent more distant star-forming regions across the Galactic plane. The resulting intrinsic pixel resolution ϑ_0 is roughly $1''.7$ and $0''.5$. For more details of the mentioned clusters in the Milky Way, see [Smith & Brooks \(2008\)](#); [Oliveira \(2008\)](#); [Megeath et al. \(2008\)](#) respectively.

7.3. Filter Bands

For the analysis of images and photometry in [Paper II](#) and [Paper III](#), we require observations in IRAC 8 μm , MIPS 24 μm , PACS 70 μm , PACS 160 μm , SPIRE 250 μm , SPIRE 350 μm and SPIRE 500 μm . For a detailed description of spectral transmission, see the [FLUXCOMPENSATOR Paper](#). We convolve the spectral cube with the transmission curves for these bands and extract 2-d images of the respective bands. We use the FLUXCOMPENSATOR’s built-in database filters. We do not take into account the effects of saturation²².

²² Note that saturation is currently not implemented in the FLUXCOMPENSATOR which might create synthetic point sources with a large dynamic range in flux. This is enhanced by the effect that in the D14 SPH simulations stars below $20 M_{\odot}$ do not ionize their surrounding or blow winds. A more realistic feedback implementation in future will improve our realistic synthetic observations.

7.4. Extinction & Background

The FLUXCOMPENSATOR can also account for effects introduced by the extinction between the simulation object and the observer. We redden the synthetic observations with the extinction law from [Kim et al. \(1994\)](#). We set the optical extinction to $A_V = 10$ mag for the distance $d = 3$ kpc and to $A_V = 20$ mag for the distance $d = 10$ kpc. See the [FLUXCOMPENSATOR Paper](#) for the description of the built-in extinction function of the FLUXCOMPENSATOR.

However, the observations are not only affected by interstellar extinction. One of the difficulties when analyzing real observations is the presence of non-uniform background, and therefore, disentangling the background from the astronomical objects is challenging. Therefore, to make sure we do not compare apples with oranges in [Paper II](#) and [Paper III](#), namely to ensure that the simulated observations are as realistic as possible, in this paper ([Paper I](#)) we attempt to combine the synthetic observations with real observations. We use relatively empty patches of the Galactic plane from the Galactic Legacy Infrared Mid-Plane Survey Extraordinaire (GLIMPSE; [Benjamin et al. 2003](#); [Churchwell et al. 2009](#)) for IRAC, from the MIPS Galactic Plane Survey (MIPSGAL; [Carey et al. 2009](#)) for MIPS, from the *Herschel* Infrared Galactic Plane Survey (Hi-GAL; [Molinari et al. 2010](#)) for PACS and SPIRE. The observations have an observed pixel resolution ϑ_{obs} of $1''.2$ (IRAC 8 μm), $2''.4$ (MIPS 24 μm), $3''.2$ (PACS 70 μm), $4''.5$ (PACS 160 μm), $6''.0$ (SPIRE 250 μm), $8''.0$ (SPIRE 350 μm) and $11''.5$ (SPIRE 500 μm). We combine relatively empty patches of real observations with our computed realistic synthetic observations for all seven bands. We place our synthetic observations roughly half a degree away ($\ell \simeq 17^{\circ}1915$, $b \simeq -0^{\circ}61870445$) from the Eagle Nebula.

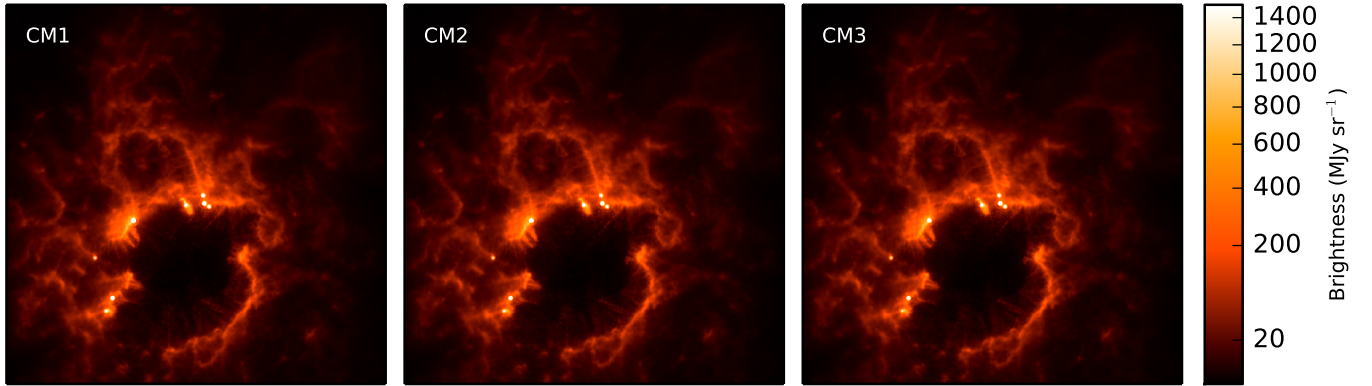


FIG. 16.— MIPS 24 μm realistic synthetic observations of different circumstellar set-ups. No additional circumstellar material (CM1), rotational flattened envelope refinement (CM2), symmetrical power-law envelope density distribution (CM3).

See the [FLUXCOMPENSATOR Paper](#) for the description of the built-in observation-combination functionality in the FLUXCOMPENSATOR.

7.5. Resolution & PSF

Since the intrinsic pixel resolution ϑ_0 is different from the observed pixel resolutions ϑ_{obs} , therefore, before we can combine the synthetic observations with real observations, we need to adjust the resolution of synthetic observations to the resolution of the real observations. We change the intrinsic pixel resolution ϑ_0 to the pixel resolution of the observations ϑ_{obs} . See the [FLUXCOMPENSATOR Paper](#) for the description of the built-in re-gridding function of the FLUXCOMPENSATOR.

To further account for diffraction, we convolve the re-gridded images in the respective bands with the point-spread-function (PSF) of the respective telescopes. See the [FLUXCOMPENSATOR Paper](#) for the description of the built-in convolution function of the FLUXCOMPENSATOR. We use the PSF files provided by the FLUXCOMPENSATOR’s built-in database.

7.6. Set of Realistic Synthetic Observations

For every selected time-step in the D14 SPH simulations, we produced realistic synthetic observations as described in Section 7, using our favored techniques presented and discussed in Section 2 to Section 6.

For the time-step 122 (6.109 Myr), we show all seven bands of the realistic synthetic observations, combined with a real observed background in Figure 15 for a distance of 3 kpc and one viewing angle. While for the IRAC, MIPS and PACS bands, the features of the simulated region dominate the image, in SPIRE the features are overpowered by the background. Clearly, this star-forming region does not contain enough mass for the SPIRE emission to dominate, when compared to the other material in the Galactic plane. Since the Galactic plane is full of clouds, other background patches within the *Herschel* Infrared Galactic Plane Survey (Hi-GAL) survey could not likely improve this. Therefore, intermediate-mass clouds, such as the simulated region here, are “lost” in SPIRE bands. This has to be kept in mind when analyzing the realistic synthetic observations in [Paper II](#) and [Paper III](#). However, we also provide the realistic synthetic observations without background. Naturally, a desired background observation in SPIRE would be slightly off the Galactic plane of a rela-

tively empty region. However, off the Galactic plane, the *Herschel* Space Observatory only observed star-forming clouds directly. We could have selected a region off the Galactic plane with lower background, but this would not have been typical of most observed star-forming regions, which at that distance are all located in the Galactic plane.

In Figure 16, we show one example for the three circumstellar set-ups described in Section 5.5. We can see that we can “observe” point sources for all three set-ups. In [Paper III](#) and [Paper IV](#), we will explore the differences when counting the young stellar population in our synthetic observations.

In Figure 17, we show an evolutionary sequence of the *run I* star-forming region of the D14 SPH simulations in PACS 70 μm at a distance of 3 kpc and for one viewing angle. We provide all (5796) realistic synthetic observations for the 3 circumstellar material set-ups, 23 time-steps, 3 viewing angles, 2 distances, 7 spectral bands and both with and without combined realistic background as FITS files in Appendix A.

8. SUMMARY

In this paper ([Paper I](#)), we produced realistic synthetic observations of the coupled high-mass stellar feedback *run I* of winds and ionization of the D14 SPH simulations. We showed that mapping of SPH particles onto a Voronoi mesh has to be done with caution. We have tested several techniques which can perform this task and found that the following methods produce the best results:

- **Pre-processing**

Different radiative transfer codes treat different physics, such as dust continuum or molecular line transfer. Therefore, it is important to filter away those SPH particles from the SPH distribution (e.g. ionized particles), which are meaningless for the radiative transfer code in question, before mapping onto the radiative transfer mesh.

- **Grid**

Within a Voronoi mesh, resolution can be increased by gradually putting in more cells at regions of interest, for instance around accreting stars. The absence of a preferred direction of the mesh creates smoother images than Cartesian grids when “observing” along a grid axis.

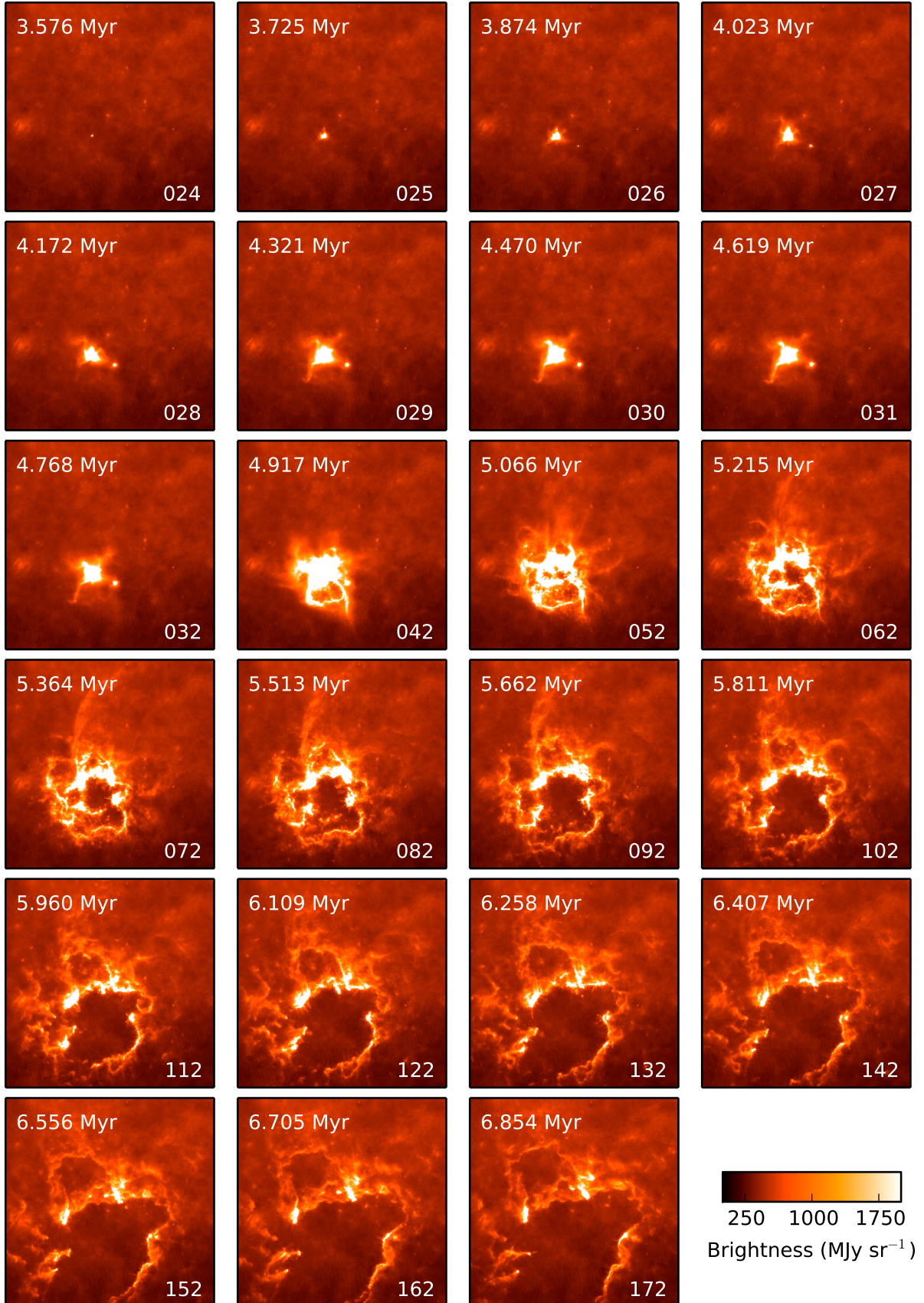


FIG. 17.— PACS 70 μm realistic synthetic observations (including background) over all time-steps of the D14 SPH simulations.

- **Sites**

When a Voronoi mesh is set up to represent an SPH simulation, including large low-density regions can cause artifacts when mapping only the positions of the SPH particles onto the mesh. Artifacts are reduced by placing Voronoi sites also at the positions of the sink particles in addition to the sites at the positions of the SPH particles. Additionally, adding circumstellar sites around the accreting sink particles reduces artifacts and increases the resolution in the circumstellar material.

- **Mapping**

The mapping of the properties, such as density and temperature, from the SPH simulation onto the radiative transfer mesh has to preserve the gradients of the original distributions. We presented a random sampling technique which ensures a smooth density and temperature mapping from the SPH simulations onto the mesh, while conserving mass.

- **Envelope Fitting**

We present three different ways of refining the circumstellar material beyond the resolution limit of the SPH simulation. We presented methods to extrapolate the inner circumstellar material with rotational flattened and spherically symmetric power-law profiles. However, inward extrapolations are only an approximation. In order to have a consistent physical picture, in future, simulations with higher resolution would be ideal.

- **Circumstellar Material**

We produced a set of realistic synthetic observations with and without circumstellar material to evaluate the impact of circumstellar material on observed fluxes. We will explore the effects on the total flux in [Paper III](#) and the point-source counting in [Paper III](#) and [Paper IV](#).

- **Dust**

To recover the NIR and MIR flux (below 70 μm), dust distributions which include PAH molecules (e.g. [Draine & Li 2007](#)) should be used when calculating the radiative transfer.

- **Temperatures**

Coupling the SPH temperature, following [Larson \(2005\)](#)'s EOS, with the iterated radiative transfer dust temperature produces unphysical emission within a dust radiative transfer code, although the hydrodynamical temperature is below the dust sublimation temperature. The line cooling part of [Larson \(2005\)](#)'s EOS causes a gas temperature rise in low density regions at the edges of the simulation, which produces unphysical/unobserved fluxes when comparing to real star-forming regions, when blindly coupling the hydrodynamical temperature with the dust radiative transfer temperature. However, the heating term in [Larson \(2005\)](#)'s EOS at low densities implies a decoupling from gas and dust. Therefore, we conclude that, at least for dust radiative transfer codes, the hydrodynamical temperature (hence gas temperature) should be replaced by a constant background temperature.

In this paper ([Paper I](#)), we will provide online about 5800 realistic synthetic observations of the 3 circumstellar material set-ups, 23 time-steps, 3 viewing angles, 2 distances, 7 spectral bands and with combined background and without of the synthetic star-forming region. The FITS files of the "observations" are stored in [Appendix A](#). In [Paper II](#), [Paper III](#) and [Paper IV](#), we will analyze these "observations".

9. ACKNOWLEDGEMENTS

We thank the referee for a constructive report that helped us improve the clarity and the strength of the results presented in our paper. This work was carried out in the Max Planck Research Group *Star formation throughout the Milky Way Galaxy* at the Max Planck Institute for Astronomy. C. K. is a fellow of the International Max Planck Research School for Astronomy and Cosmic Physics (IMPRS) at the University of Heidelberg, Germany and acknowledges support. C. K. acknowledges support from STFC grant ST/M001296/1. J. E. D. was supported by the DFG cluster of excellence *Origin and Structure of the Universe*. This research made use of Astropy, a community-developed core Python package for Astronomy ([Astropy Collaboration et al. 2013](#)), matplotlib, a Python plotting library ([Hunter 2007](#)), Scipy, an open source scientific computing tool ([Jones et al. 2001](#)–), the NumPy package ([van der Walt et al. 2011](#)) and IPython, an interactive Python application ([Pérez & Granger 2007](#)).

REFERENCES

- Armitage, P. J. 2010, *Astrophysics of Planet Formation*, 1st edn. (Cambridge University Press)
- Astropy Collaboration, Robitaille, T. P., Tollerud, E. J., et al. 2013, *A&A*, 558, A33
- Barcarolo, D., Le Touzé, D., OGER, G., & De Vuyt, F. 2014, in 9th Int. SPHERIC Workshop, Paris, France
- Bate, M. R. 2014, *MNRAS*, 442, 285
- Bate, M. R., Bonnell, I. A., & Bromm, V. 2002a, *MNRAS*, 332, L65
- . 2002b, *MNRAS*, 336, 705
- . 2003, *MNRAS*, 339, 577
- Bate, M. R., Bonnell, I. A., & Price, N. M. 1995, *MNRAS*, 277, 362
- Benjamin, R. A., Churchwell, E., Babler, B. L., et al. 2003, *PASP*, 115, 953
- Bernasconi, P. A., & Maeder, A. 1996, *A&A*, 307, 829
- Brott, I., & Hauschildt, P. H. 2005, in *ESA Special Publication*, Vol. 576, *The Three-Dimensional Universe with Gaia*, ed. C. Turon, K. S. O'Flaherty, & M. A. C. Perryman, 565
- Camps, P., Baes, M., & Saftly, W. 2013, *A&A*, 560, A35
- Carey, S. J., Noriega-Crespo, A., Mizuno, D. R., et al. 2009, *PASP*, 121, 76
- Carroll, B. W., & Ostlie, D. A. 1996, *An Introduction to Modern Astrophysics*, 1st edn. (Addison Wesley Publishing Company)
- Castelli, F., & Kurucz, R. L. 2004, *ArXiv Astrophysics e-prints*, astro-ph/0405087
- Churchwell, E., Babler, B. L., Meade, M. R., et al. 2009, *PASP*, 121, 213
- Dale, J. E. 2015, *New Astronomy Reviews*, 68, 1
- Dale, J. E., & Bonnell, I. 2011, *MNRAS*, 414, 321
- Dale, J. E., & Bonnell, I. A. 2008, *MNRAS*, 391, 2
- Dale, J. E., Ercolano, B., & Bonnell, I. A. 2012, *MNRAS*, 424, 377


```

O1      : <orientation plane>      # O1 (xy), O2 (xz), O3(yz)
D1      : <distance>                # D1 (3kpc), D2 (10kpc)
MIPS1   : <detector>               # Detector of realistic synthetic observation
R1      : <resolution type>        # detector resolution (R1),
                                     # technique resolution (R2)
B2      : <background type>        # without background (B1),
                                     # with background (B2)

```

The different methods and their abbreviations are described in [Paper I](#). In the header of the respective FITS file, the information from the file name is stored additionally. The FITS files include world coordinate information similarly to real observations from the respective detectors. As an example, we show the FITS header of a MIPS 24 μm observation below:

```

SIMPLE =          T / conforms to FITS standard
BITPIX =         -64 / array data type
NAXIS  =          2 / number of array dimensions
NAXIS1 =          860
NAXIS2 =          860
WCSAXES =         2 / Number of coordinate axes
CRPIX1 =        -781.75 / Pixel coordinate of reference point
CRPIX2 =         1358.25 / Pixel coordinate of reference point
CDELTA1 =    -0.0006666666666666 / [deg] Coordinate increment at reference point
CDELTA2 =     0.0006666666666666 / [deg] Coordinate increment at reference point
CUNIT1  = 'deg' / Units of coordinate increment and value
CUNIT2  = 'deg' / Units of coordinate increment and value
CTYPE1  = 'GLON-CAR' / galactic longitude, plate caree projection
CTYPE2  = 'GLAT-CAR' / galactic latitude, plate caree projection
CRVAL1  =          18.0 / [deg] Coordinate value at reference point
CRVAL2  =          0.0001 / [deg] Coordinate value at reference point
LONPOLE =          0.0 / [deg] Native longitude of celestial pole
LATPOLE =         89.9999 / [deg] Native latitude of celestial pole
BUNIT   = 'MJy/sr' / Units of array
DISTANCE =          3.0 / Distance to object in units of kpc
FEEDBACK = 'both' / High-mass stellar feedback
RUNTYPE  = 'I' / SPH simulation set-up type
TIMESTEP = '122' / SPH simulation time-step
SITETYPE = 's3' / Site distribution: s1, s2, s3
PARATYPE = 'p3' / Parameter mapping: p1, p2, p3
GRIDTYPE = 'voronoi' / Grid types: Voronoi tessellation
DUSTTYPE = 'DraineLiPAH' / Dust types: DraineLiPAH, DraineMW
CLIPTYPE = 'c1' / Clipping SPH sample: c1, c2
DTYPE   = 'DT2' / Radiative transfer set-up: DT1, DT2, DT3
CMTYPE  = 'CM1' / Circumstellar material: CM1, CM2, CM3
ORIETYPE = 'O1' / Orientation plane: O1 (xy), O2 (xz), O3(yz)
DISTTYPE = 'D1' / Distance: D1 (3kpc), D2 (10kpc)
RITCODE = 'HYPERION' / 3-d dust continuum radiative transfer code
SYNOBS  = 'FluxCompensator' / Tool to create realistic synthetic observations
DETECTOR = 'MIPS1' / Detector of realistic synthetic observations
RESTYPE  = 'R1' / Resolution type: R1 (detector), R2 (other)
BGTYPE  = 'B2' / Background type: B1 (without), B2 (with)
COMMENT For more description see Appendix.
END

```

RANDOM SAMPLING WITH PROBABILITY DISTRIBUTION FUNCTIONS

A PDF is dependent on a variable x that we want to distribute. A random number ξ is sampled between $[0, 1]$ and the distributed variable $x(\xi)$ is equated through analytical or numerical integration of the PDF through inverse transform sampling (for more information on PDFs, see [Press et al. 1992](#)):

$$\xi = \frac{\int_{x_{min}}^x P(x') dx'}{\int_{x_{min}}^{x_{max}} P(x') dx'} \rightarrow x(\xi) \quad (\text{B1})$$

Following Section 3.2.3, we can sample the radial log-spaced PDF through a step-by-step evaluation of the integral over the normalized PDF. The log-spaced probability distribution produces more sites at small radii. Hence, the size of the Voronoi cells will decrease and we recover a smoother gradient of density across the dynamic range (this will be discussed further in Section 5.1). With a constant PDF = $const = c$, we can solve the integral for the radius r

analytically using inverse transform sampling:

$$\xi = \int_{r_{min}}^r d \log_{10}(r) \text{PDF} \stackrel{\text{PDF}=c}{=} c \int_{r_{min}}^r d \log_{10}(r) = c [\log_{10} r - \log_{10} r_{min}] \quad (\text{B2})$$

$$r = 10^{\xi/c + \log_{10} r_{min}}.$$

Eq. B2 uses the random numbers ξ from 1 to zero and the normalization constant c

$$1 = \int_{r_{min}}^{r_{max}} d \log_{10}(r) \text{PDF} \stackrel{\text{PDF}=c}{=} c \int_{r_{min}}^{r_{max}} d \log_{10}(r) = c [\log_{10} r_{max} - \log_{10} r_{min}] \quad (\text{B3})$$

$$c = 1 / [\log_{10} r_{max} - \log_{10} r_{min}], \quad (\text{B4})$$

to calculate the distribution function:

$$r = 10^{\xi[\log_{10} r_{max} - \log_{10} r_{min}] + \log_{10} r_{min}}. \quad (\text{B5})$$

Following Section 3.3.2, to space the split SPH particle k with respect to the SPH particle i again, we use the PDF (as in Eq. B2). However, this time the

$$\text{PDF} = \tilde{c} W_{ik}(r_{ik}, h_i) \neq \text{const} \quad (\text{B6})$$

with the spacing r_{ik} and the SPH particle smoothing length h_i . We determine the spacing r_{ik} , by setting up the integral over the PDF (i. e. Eq. B2) but this time with linear spacing:

$$\xi = \int_{r_{min}}^{r_{ik}} dr r^2 \text{PDF} = \tilde{c} \int_{r_{min}}^{r_{ik}} dr r^2 W_{ik}(r_{ik}, h_i = 1) \quad (\text{B7})$$

for a constant smoothing length $h_i = 1$, with the random numbers ξ and the normalizing constant \tilde{c} . Since the PDF is not constant, we have to solve for the values of distance r_{ik} numerically (see Press et al. 1992).

SPECTRA INTERPOLATION

Following Section 4.2, we will describe here in more detail the spectra interpolation. We pick the four closest model spectra $F_{\text{mod}}(T_1, T_2, g_1, g_2)$, which have values between

$$\log_{10} T_2 \geq \log_{10} T_{\text{eff}} \geq \log_{10} T_1 \quad (\text{C1})$$

$$\log_{10} g_2 \geq \log_{10} g_* \geq \log_{10} g_1 \quad (\text{C2})$$

and define the model differences as follows:

$$\Delta T = \log_{10} T_2 - \log_{10} T_1 \quad (\text{C3})$$

$$\Delta g = \log_{10} g_2 - \log_{10} g_1 \quad (\text{C4})$$

$$\Delta T_e = \log_{10} T_2 - \log_{10} T_{\text{eff}} \quad (\text{C5})$$

$$\Delta g_* = \log_{10} g_2 - \log_{10} g_*. \quad (\text{C6})$$

Through bilinear interpolation (for more details, see Press et al. 1992), we weight the four spectra

$$F_{\text{mod}} = \begin{pmatrix} F_{\text{mod}}(T_1, g_1) & F_{\text{mod}}(T_1, g_2) \\ F_{\text{mod}}(T_2, g_1) & F_{\text{mod}}(T_2, g_2) \end{pmatrix} \quad (\text{C7})$$

with the differences from Eq. C3 to Eq. C6 and extract the spectra F_{ν^*} of a source with mass M_* :

$$F_{\nu^*} = (\Delta T_e \ \Delta T \ - \ \Delta T_e) \frac{F_{\text{mod}}}{\Delta T \Delta g} \begin{pmatrix} \Delta g_* \\ \Delta g - \Delta g_* \end{pmatrix}. \quad (\text{C8})$$